Engineering Structures 252 (2022) 113621

Contents lists available at ScienceDirect

Engineering Structures

journal homepage: www.elsevier.com/locate/engstruct

Experimental and numerical investigations on RC beams with stirrups scaled along height or length

I. Marzec, J. Tejchman *

Gdansk University of Technology, Gdańsk-Wrzeszcz 80-233, Narutowicza 11/12, Poland

ARTICLE INFO

Keywords:
Reinforced concrete beams
Stirrups
Shear strength
Finite element method
Elasto-plasticity-damage
Non-local theory

ABSTRACT

Reinforced concrete (RC) beams with transverse reinforcement (stirrups) subjected to four-point bending were experimentally and numerically investigated. Beams were scaled along the height or length. They were over-reinforced to avoid longitudinal bars' yielding. First, laboratory tests on RC beams with stirrups were conducted. Due to the lack of a geometrical similarity, two separate failure modes were observed depending upon the ratio of the shear span to the beam depth $\eta_a = a/D$. In experiments, a shear-compression failure mode dominated for small values of η_a, and concrete crushing in a beam compression zone prevailed for high values of η_a. Next, the finite element method (FEM) was used in calculations to directly simulate the experiments. A coupled isotropic elasto-plastic-damage constitutive model for concrete under plane stress conditions was adopted. The constitutive model was enhanced by integral-type non-locality in the softening regime to provide mesh-objective results. A bond-slip law was assumed between concrete and longitudinal bars. Numerical simulations under plane stress conditions satisfactorily reproduced the experimental shear strengths and failure modes for all beams with the same set of input parameters. A wide parametric study regarding the numerical influence of the longitudinal and transverse reinforcement ratio and shear span parameter on beam strength and failure mode was performed. In addition, one full three-dimensional (3D) calculation was also carried out for comparative purposes.

1. Introduction

A size effect is an inherent characteristic of all semi-brittle materials such as concrete subjected to increasing load till its maximal value and continuing in a post-critical softening regime under displacement control. It denotes reduction of the nominal structural strength (referred to maximal load value) and reduction of ductility (measured by the ratio of the load work in the post-critical regime to the total work in the deformation process) with growing structural element size [1]. These two properties are of significant importance for the evaluation of element safety. The size effect is caused by intense strain localization regions of a certain volume which precede the occurrence of discrete macro-cracks (their size related to a characteristic member size contributes to a deterministic size effect) and by a spatial variability/randomness of local material properties (contributing to a statistical size effect that becomes dominant with increasing characteristic size of members). Since the strain localization zone size, which is sensitive to the ratio between the size of strain localization zones and the specimen size, cannot be experimentally scaled in laboratory tests. Concrete elements indicate a transition from a snap-through response in the post-critical regime for small-size elements to a snap-back response (a catastrophic drop in strength related to a positive slope in a stress–strain softening branch) for large-size elements. There exist several size effect rules for concrete elements for geometrically similar structures [1–4] for which the same failure mode occurs for a varying scalar size parameter. The most realistic is the combined energetic-statistical size effect rule proposed by Bazant [4]. However, structure shape, reinforcement layout and size variation can depend on several parameters, which is typical in the design process. Thus, differing failure modes may occur and each mode is characterized by a different strength reduction rule depending on the growth/decrease of the specific design parameter. It is thus desired to investigate the extended dependence of nominal strength on both the size parameter (as in the size effect for geometrically similar elements) and non-dimensional geometric parameters (e.g. size ratio) and to derive a size effect dependent on those geometric parameters (if they are variable). In our studies, the RC beams with independent variations of length and depth were tested and the transition from flexural to shear failure modes was considered with differing expressions for

---

* Corresponding author.
E-mail addresses: irek@pg.edu.pl (I. Marzec), tejchmk@pg.edu.pl (J. Tejchman).

https://doi.org/10.1016/j.engstruct.2021.113621
Received 10 June 2021; Received in revised form 26 October 2021; Accepted 16 November 2021

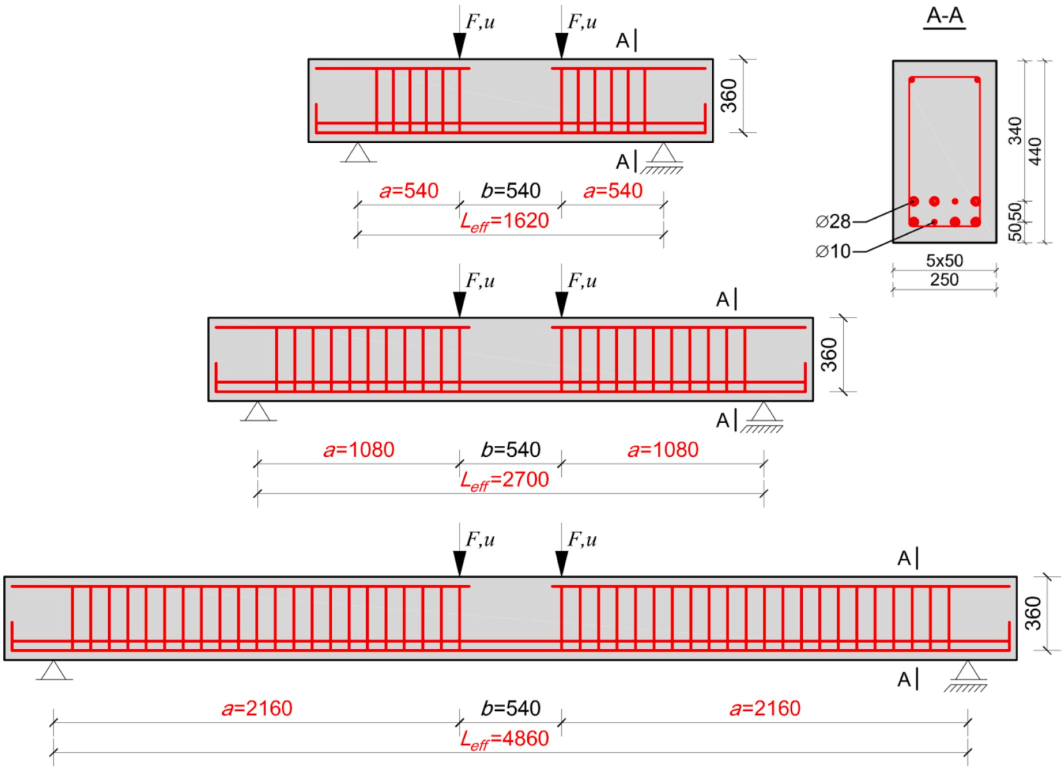

Fig. 1. Experimental reinforced concrete beams of series ‘3’ under four-point bending [22]: geometry, reinforcement arrangement, loading scheme and cross-section.

strength dependence on beam length and beam depth parameter values. Such a multi-parameter approach seems to provide more useful information on structural strength than the developed study of a single-size parameter effect.

There exist extensive experiments of a size effect for geometrically similar RC beams (with the same failure mechanism). A strong size effect was experimentally observed in RC beams without shear reinforcement during diagonal shear-tensile failure (e.g. [5–14]). The size effect was mainly of the deterministic type [1]. The size effect was also observed in reinforced concrete beams with shear reinforcement [15–17]. In these experiments, a diagonal shear-tensile fracture [15,16] or crushing of a compressive zone [17] took place in concrete. Thus, the use of stirrups did not suppress the size effect provided the longitudinal and vertical reinforcement yielding did not occur. The effect of the varying reinforcement ratio on the failure mode in RC beams was experimentally shown by Carpintieri et al. [18]. The observed failure mode changed from longitudinal reinforcement yielding, through diagonal tension to compressive zone crushing with increasing reinforcement ratio. However, only a few papers were devoted to the behaviour of RC beams with independently varying heights and lengths (e.g. [19,20]).

In a previous paper published by the authors [20], the extensive laboratory experiments on longitudinally reinforced concrete beams without shear reinforcement subjected to four-point bending were described. RC beams of separately varying height and length were experimentally analyzed concerning the nominal strength and post-critical brittleness. Beams were scaled in the height direction in the first test series and the length direction in the second test series. Two failure mechanisms were exhibited: flexural failure mechanism with plastic yielding of reinforcement and brittle shear mechanism in concrete with dominant normal diagonal crack displacements (so-called shear-tension failure mode) or with simultaneous significant normal and tangential diagonal crack displacements (so-called shear-compression failure mode). Next, the experiments were simulated with the finite element method (FEM) under plane stress conditions, with the use of an isotropic elasto-plastic-damage formulation with non-local softening [21]. The bond-slip law was assumed in FE analyses between concrete and reinforcement. A satisfactory agreement between numerical and experimental results was achieved concerning both the shear strength and failure mechanism. The FE results were insensitive to the finite element mesh size and alignment due to the presence of a characteristic length of micro-structure, introduced with the aid of integral-type non-locality in a softening regime. The current paper continues the experiments [20] and calculations [21] by the authors on RC beams without shear reinforcement, however this time the RC beams also included shear reinforcement.

The main aim of our research works was to show the effect of the shear span ratio, main and secondary reinforcement ratio on strength and a failure mode of RC beams including shear reinforcement (with an independently varying height and length) by means of a simple diagram, which is of importance in the design process. Such a useful diagram does not exist in the literature yet. Since the existing simplified design approaches are not able to properly predict both the shear strength and a failure mode, we decided to use a realistic finite element model to construct such a diagram (the numerical model was validated by experiments). First, the paper presents some experimental results on RC beams with shear reinforcement under four-point bending [22]. The geometry of beams in the current study was similar to those in [20] for comparative purposes. As compared to [15–17], the experiments in the current paper on non-geometrically similar RC beams were more comprehensive since they: 1) included various failure mechanisms, 2) took into account a change of both the effective depth or length and 3) directly compared beams with and without stirrups. Second, the experiments were numerically simulated with FEM under plane stress conditions, based on the same constitutive model for concrete as in [21] to check its capability to reproduce also the behaviour of RC beams possessing vertical reinforcement. The focus was on the faithful reproduction of different failure modes, maximum vertical forces, location, inclination and spacing of failure localized zones obtained in the experiments. Since large-scale experiments on concrete or RC concrete elements are costly as compared to numerical calculations, it is desired

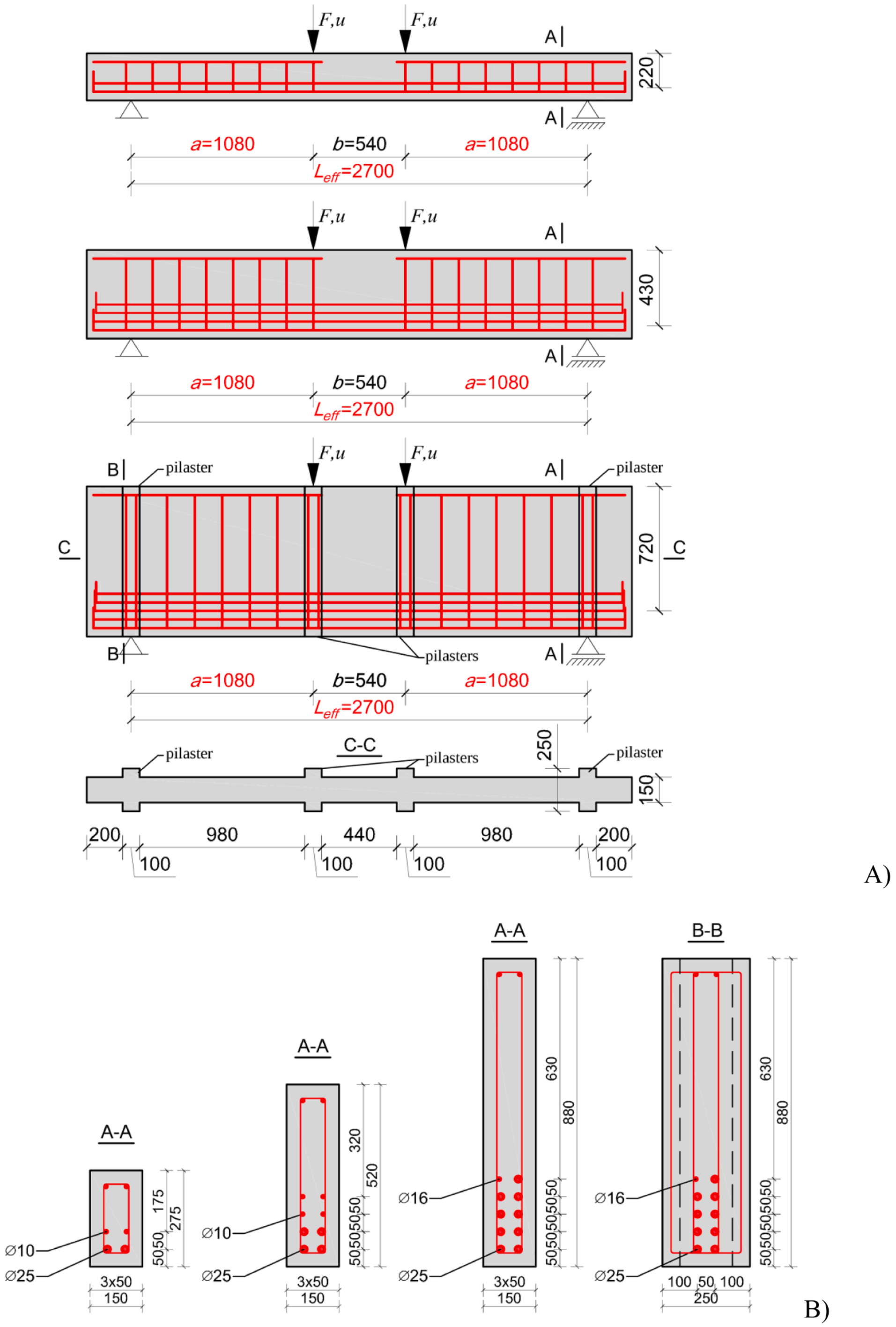

Fig. 2. Experimental reinforced concrete beams of series ‘4’ under four-point bending [22]: A) geometry, reinforcement arrangement, loading scheme and B) cross-sections.

to formulate a realistic numerical concrete model for describing the beam behaviour by taking into account the influence of different parameters, such as dimensions of RC elements, shear span, main and secondary reinforcement ratio, tensile and compressive strength of concrete et ca. After validating the numerical model, based on experiments, comprehensive numerical FE analyses were finally carried out for investigating the influence of the shear span, main and secondary reinforcement ratio on strength and a failure mode. In summary, the novel points of our research works are: 1) experiments on large non-geometrically similar RC beams with stirrups, taking into account a change of both the effective depth or length (that were not performed yet) and 2) presentation of a 3D diagram showing the effect of the shear span ratio, main and secondary reinforcement ratio on strength and a failure mode of RC beams, based on comprehensive numerical FE simulations using a constitutive model for concrete that was validated with the aid of experiments. The numerical model properly captures strain localization and is able to distinguish between different failure modes such as shear compression, shear tension and concrete crushing. Such a diagram was not shown in the literature yet.

The structure of the paper is the following. After Introduction (Section 1), the experimental results on RC beams with shear reinforcement are summarized in Section 2. In Section 3, FE modelling of concrete,

Table 1
Dimensions of reinforced concrete beams with stirrups in series ’3’ and ‘4’ [22].

Beam dimension	D [mm]	L_{eff} [mm]	a [mm]	b [mm]	t [mm]	$\eta_a = a/D$	$\eta_L = L_{eff}/D$	$\eta_b = b/D$
Series 3 S3D36A54	360	1620	540	540	250	1.5	4.5	1.5
Series 3 S3D36A108	360	2700	1080	540	250	3.0	7.5	1.5
Series 3 S3D36A216	360	4860	2160	540	250	6.0	13.5	1.5
Series 4 S4D22A108	220	2700	1080	540	150	5.0	12.3	2.5
Series 4 S4D43A108	430	2700	1080	540	150	2.5	6.3	1.25
Series 4 S4D72A108	720	2700	1080	540	150	1.5	3.75	0.75

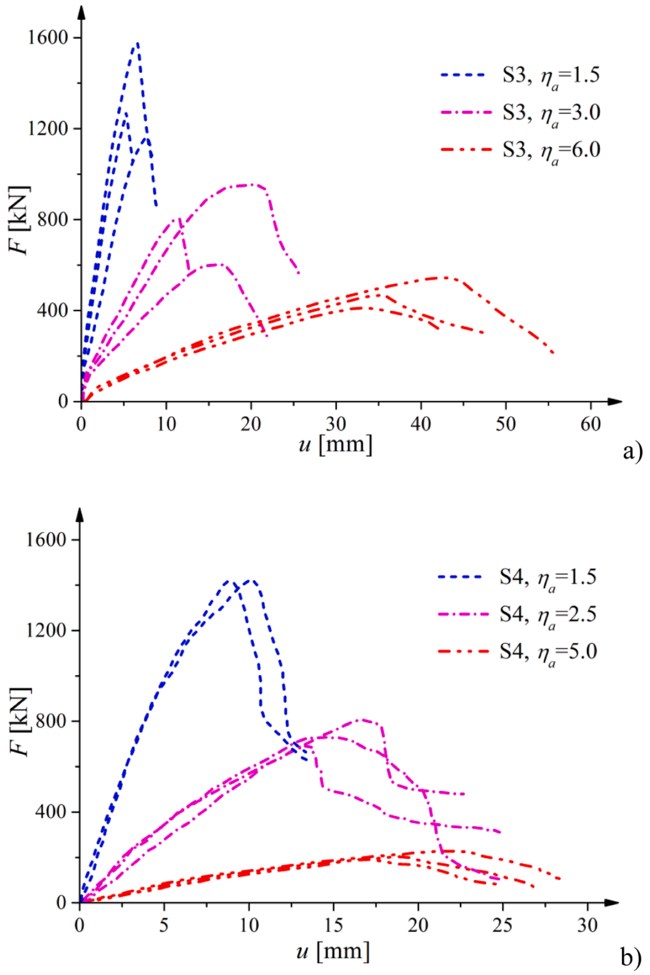

Fig. 3. Experimental vertical force–deflection $F = \mathrm{f}(u)$ curves of RC beams with stirrups of series ‘3’(a) and series ‘4’ (b) with different parameter $\eta_a = a/D$ [22] (D - effective depth and a - shear span).

reinforcement and bond-slip is introduced. Section 4 describes FE analysis results of RC beams with stirrups. The comparison of shear strengths between experimental, numerical and analytical results is discussed in Section 5. The comparative 3D results for one RC beam are shown in Section 6.1. Some additional parametric studies regarding the influence of the main and secondary reinforcement ratio and shear span parameter on strength and failure modes of beams in 2D are presented in Section 6.2. The conclusions are offered in Section 7.

2. Experiments

2.1. *RC beam geometry and material properties*

All RC beams were symmetrically loaded by two vertical concentrated forces at the distance a from both supports (a denotes the shear zone region) and had the constant bending moment zone b in the beam central part. The beams were scaled along with either the effective length L_{eff} (series ‘3’, Fig. 1) or effective depth D (series ‘4’, Fig. 2) [22]. The RC beams without stirrups were denoted as the series ‘1’ and series ‘2’ [20]. The beams of the series ‘3’ and ‘4’ were cast separately, however, the concrete recipe was similar. The maximum aggregate diameter was $d_{max} = 16$ mm. The concrete specimens were cut out from the damaged beams after experiments to verify the compressive strength. The mean strength f_{cm} (determined on cylinders ϕ100 mm) of the beams S3D36A108_2 and S3D36A54_2 was made of weaker concrete $f_{cm} = 39$ MPa than the other ones. The remaining beams had the strengths $f_{cm} = 58$ MPa and $f_{cm} = 56$ MPa in the series ‘3’ and series ‘4’, respectively. The guaranteed yield strength of longitudinal and shear reinforcement was 560 MPa. The shear span parameter $\eta_a = a/D$ changed between 1.5 and 6 to find as in [20] transitory points of failure mode changes (reinforcement yielding, shear failure and concrete crushing).

2.1.1. *RC beams of series ‘3’: Varying shear span a*

The RC beams in the series ‘3’ had the constant effective depth $D = 360$ mm but the varying shear span $a = 540$, 1080 and 2160 mm (Fig. 1, Table 1) [22]. The shear span parameter $\eta_a = a/D$ changed from 1.5 through 3 up to 6. The thickness of all beams in the series ‘3’ was $t = 250$ mm. The main reinforcement ratio of all over-reinforced beams was $\rho_l = 4.3\%$ (consisted mainly of longitudinal steel ribbed bars of the diameter 28 mm and also of the diameter 10 mm) and the shear reinforcement ratio was $\rho_s = 0.4\%$ (designed as two-legged closed stirrups of the diameter ϕ8). Next, the same reinforcement ratio was adopted for other RC beams. The beams were denoted as S3D36A54, S3D36A108 and S3D36A216 (where S denotes the series number, D - the effective depth in [cm] and A - the shear span length in [cm]). Three identical specimens were prepared for each beam size (the specimen number is attached at the end of the beam symbol e.g. S3D36A54_1). In total, 9 RC beams were tested in the series ‘3’. The beams in the series ‘3’ had a significantly higher longitudinal reinforcement ratio ($\rho_l = 4.3\%$) than previously tested beams without shear reinforcement in the series ‘2’ ($\rho_l = 1.4\%$) [20]. This unusually high ρ_l was required to prevent main reinforcement yielding. . The value of $\rho_l = 4.3\%$ was analytically determined for the longest beam in the series ‘3’ to obtain concrete crushing (based on a force equilibrium in the beam cross-section) [22]. Next, the same reinforcement ratio was adopted for other RC beams. Furthermore, the beams in the series ‘3’ had the designed shear span parameters η_a different from the beams in the series ‘2’ to observe a varying failure mechanism. Another determinant for the beam geometry was the upper load limit of the testing machine in the laboratory (about 1800 kN). Due

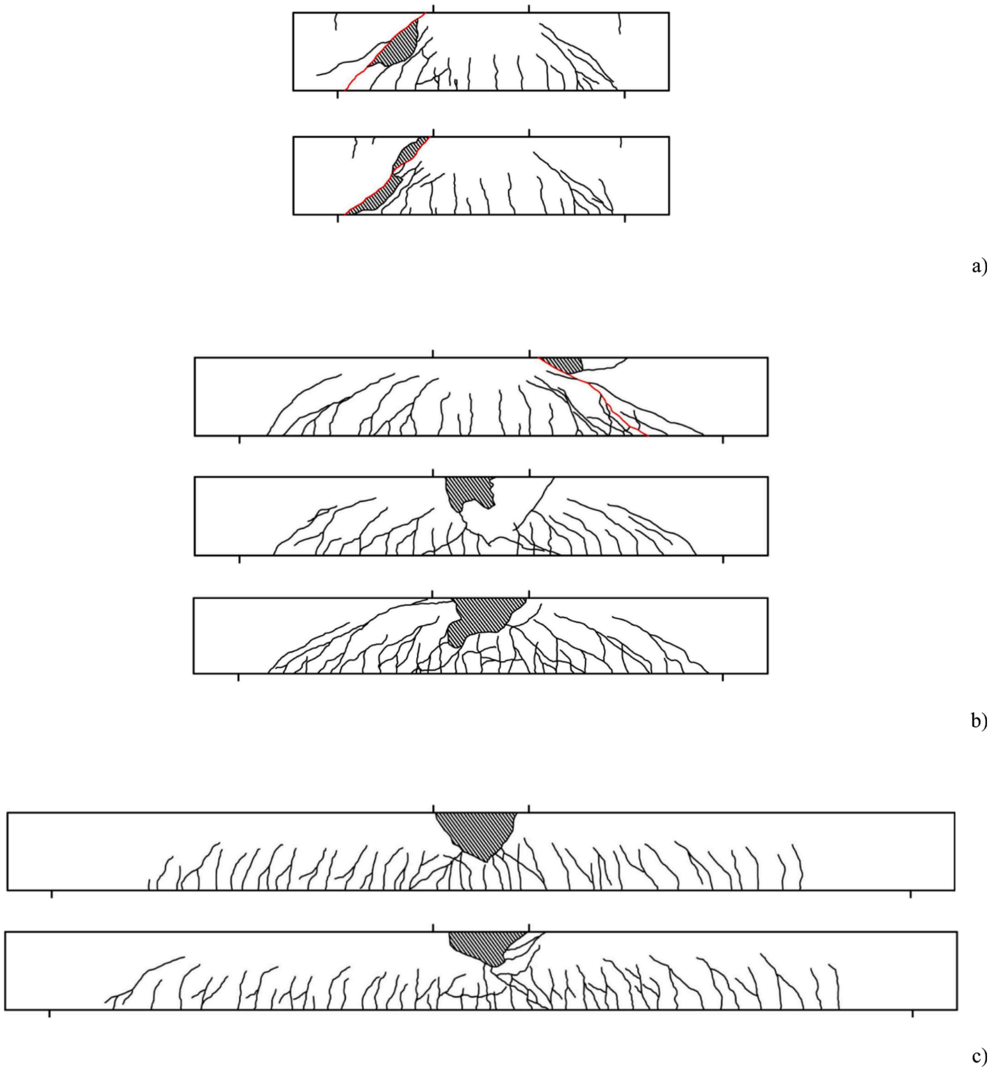

Fig. 4. Crack patterns at failure typical for RC beams with stirrups (series ‘3’) [22]: a) beams S3D36A54 ($\eta_a = 1.5$), b) S3D36A108 ($\eta_a = 3.0$) and c) S3D36A216 ($\eta_a = 6.0$).

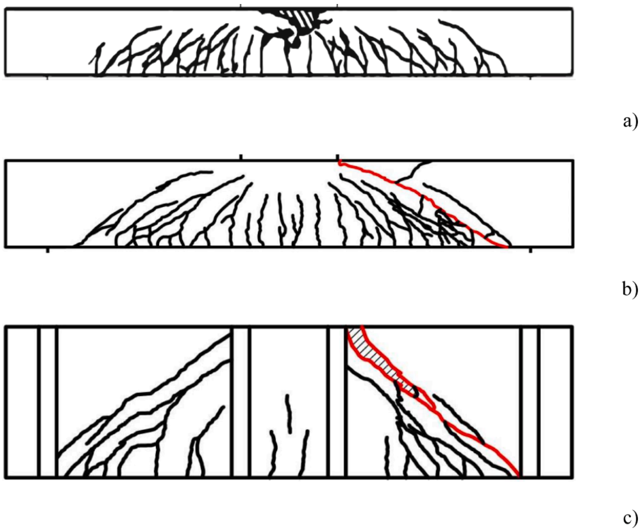

Fig. 5. Crack patterns at failure typical for RC beams with stirrups (series ‘4’) [22]: a) beam S4D22A108 ($\eta_a = 5.0$), b) S4D43A108 ($\eta_a = 2.5$), and c) S4D72A108 ($\eta_a = 1.5$).

to that limit, the shortest beam with stirrups in the series ‘3’ had the parameter $\eta_a = 1.5$ instead of $\eta_a = 1.0$ (as the shortest beam without stirrups in the series ‘2’ [20]. The area of the loading/supporting plates was 100 × 250 mm^2.

2.1.2. RC beams of series ‘4’: Varying effective beam depth D

The RC beams in the series ‘4’ had the varying effective depth D = 220, 430 and 720 mm but the constant shear span a = 1080 mm (Fig. 2, Table 1) [22]. The shear span parameter $\eta_a = a/D$ changed from 1.5 through 2.5 up to 5. The beams were denoted as S4D22A108, S4D43A108 and S4D72A108. The thickness of all beams in series ‘3’ was reduced from t = 250 mm down to t = 150 mm due to the load limit of the testing machine (the effect of a beam thickness is usually negligible [22,23]). The beam S4D72A108 compromised 3 identical prismatic trial specimens (denoted as S4D72A108_T1 - S4D72A108_T3) and 2 specimens with additional strengthening pilasters in the axes of external forces (S4D72A108_1 - S4D72A108_2) to avoid local concrete crushing at all loading/supporting points. Each of the beams S4D22A108 and S4D43A108 were represented by 3 identical specimens. In total, 9 RC beams were tested in the series ‘4’. The area of the loading/supporting plates was 100 × 150 mm^2. The shear span parameters $\eta_a = 2.5$ and 5 in the beams from the series ‘4’ slightly differed from the beams in the series ‘3’ with $\eta_a = 3$ and 6. This unintended discrepancy came out from

Table 2
Experimental failure force $F_{max} = 2P_{max}$ and shear failure stress $\nu = P_{max}/(tD)$ for two failure modes with RC beams including stirrups of series '3' and series '4' [22] (*CC* - concrete crushing in compressive zone and *SC* - shear-compression failure).

Beam no	'1' F_{max} [kN]/ failure mode	'2' F_{max} [kN]/ failure mode	'3' F_{max} [kN]/ failure mode	Mean value F_{max}[kN]	Mean value ν[MPa]
Series 3 S3D36A216 $\eta_a = 6.0$, $\eta_b = 1.5$	544/CC	411/CC	469/CC	475	2.64
Series 3 S3D36A108 $\eta_a = 3.0$, $\eta_b = 1.5$	802/SC	601/CC	954/CC	878*	4.88*
Series 3 S3D36A54 $\eta_a = 1.5$, $\eta_b = 1.5$	1574/SC	1165/SC	1271/SC	1423*	7.43*
Series 4 S4D22A108 $\eta_a = 5.0$, $\eta_b = 2.5$	227/CC	204/CC	191/CC	207.4	3.17
Series 4 S4D43A108 $\eta_a = 2.5$, $\eta_b = 1.5$	694/SC	808/SC	732/CC	744.4	5.76
Series 4 S4D72A108 $\eta_a = 1.5$, $\eta_b = 0.75$	1420/SC	1416/SC	1423/SC	1420	6.52

* Average value without beams made of weaker concrete.

a faulty performance of beam heights *H* (and *D*) in a prefabrication factory. The longitudinal reinforcement consisted of steel ribbed bars of diameter 10, 16 and 25 mm (Fig. 2) while the shear reinforcement was made of two-legs closed stirrups of diameter 8 mm. Due to the incorrect beam effective depths *D,* the main reinforcement ratio diverged from the assumed one. The beam S4D72A108 had again the high longitudinal reinforcement ratio $\rho_l = 4.3\%$ (similar to beams in the series '3') whereas the beams S4D22A108 and S4D43A108 had $\rho_l = 3.5\%$. This slightly lower main reinforcement ratio did not affect the expected experimental failure mode since it was still sufficient to prevent steel yielding. The bar diameter was mainly 25 mm and also 10 mm. The shear reinforcement ratio was always $\rho_s = 0.4\%$.

2.2. Experimental results on strength and fracture

The experimental load–deflection diagrams $F = f(u)$ are shown in Fig. 3 (*F* - vertical force and *u* - deflection) [22]. Figs. 4 and 5 show the crack patterns in RC beams and Table 2 includes the failure forces $F_{max} = 2P_{max}$ and the corresponding shear failure stresses $\nu = P_{max}/(tD)$ from the experiments [22]. The shear span parameter $\eta_a = a/D$ was germane for the beam strength, brittleness and failure mode.

2.2.1. RC beams of series '3': Varying shear span ($\rho_l = 4.3\%$, $\rho_s = 0.4\%$)

The longest beams S3D36A216 with $\eta_a = 6$ always failed due to concrete crushing (C) in the constant bending moment zone (Fig. 4) since both flexural and shear reinforcement was sufficient to resist the critical bending and shear stresses [22]. The averaged ultimate vertical force for S3D36A216 beams was 473.7 kN (Fig. 3a, Table 2). All beams of this type had similar normalized load–deflection paths including the registered post-peak brittleness resulting from the compressive concrete behaviour in the softening regime (Fig. 3a). The beams S3D36A108 with $\eta_a = 3$ constituted a transitional geometry between two different failure mechanisms. The beam S3D36A108_1 failed in shear-compression (SC)

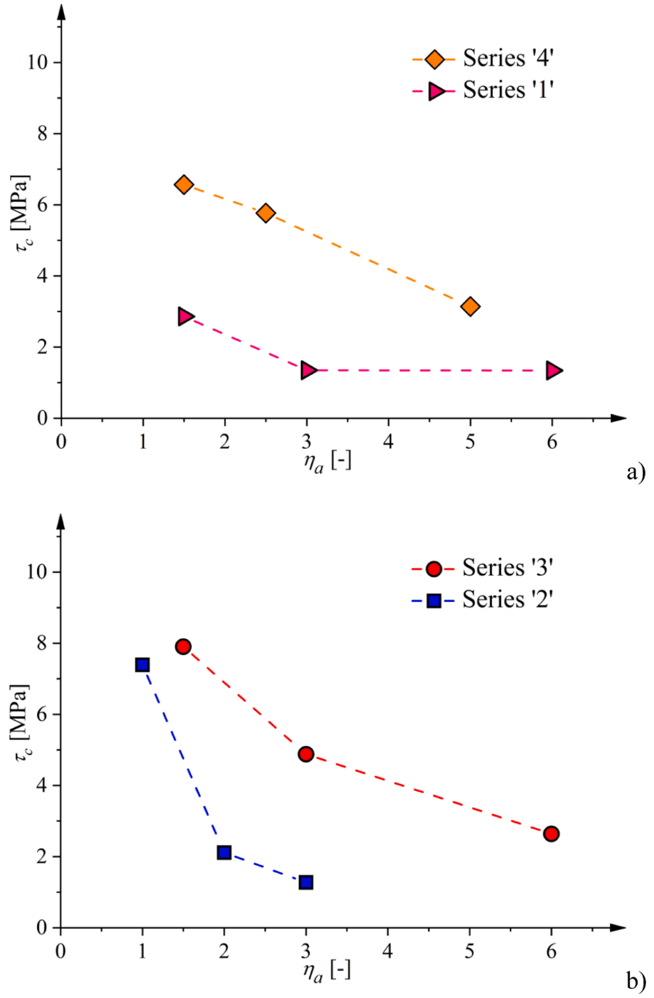

Fig. 6. Average ultimate shear stress in beams with shear reinforcement (series '3' and series '4', [22]) and without shear reinforcement (series '1' and series '2', [20]) with varying parameter $\eta_a = a/D$ (*D* - effective depth and *a* - shear span).

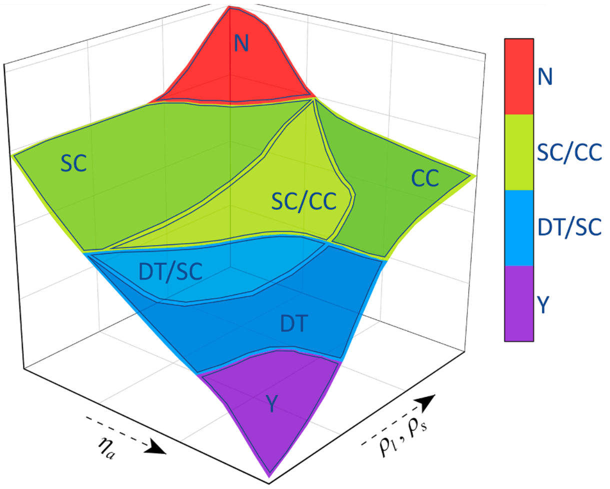

Fig. 7. Regions of failure modes of RC beams with/without stirrups of varying geometry (*a*, *D*) and reinforcement ratios ρ_l and ρ_s [22] (Y - reinforcement yielding, DT - diagonal tension, SC - shear-compression, CC - concrete crushing and N –support zone crushing, *a* - shear span, *D* - beam depth, ρ_l - longitudinal reinforcement ratio and ρ_s - vertical reinforcement ratio).

Table 3

Material constants assumed in FE calculations for concrete.

	Material constants for concrete	
Elasticity	Modulus of elasticity E (GPa)	34
	Poisson's ratio ν (–)	0.2
Plasticity	Internal friction angle ϕ (°)	14
	Dilatancy angle ψ (°)	8
	Plastic hardening modulus (GPa)	18
Damage	Initial yield stress (tension) $\sigma_{yt}{}^{0}$ (MPa)	3.1
	Initial yield stress (compression) $\sigma_{yc}{}^{0}$ (MPa)	58
	State variable κ_0 (–)	8.6×10^{-5}
	Damage parameter (tension) α (–)	0.95
	Damage parameter (tension) β (–)	85
	Damage parameter (compression) η_1 (–)	1.15
	Damage parameter (compression) η_2 (–)	0.15
	Damage parameter (compression) δ_c (–)	150
	Splitting factor a_c [–]	1
	Splitting factor a_t [–]	0

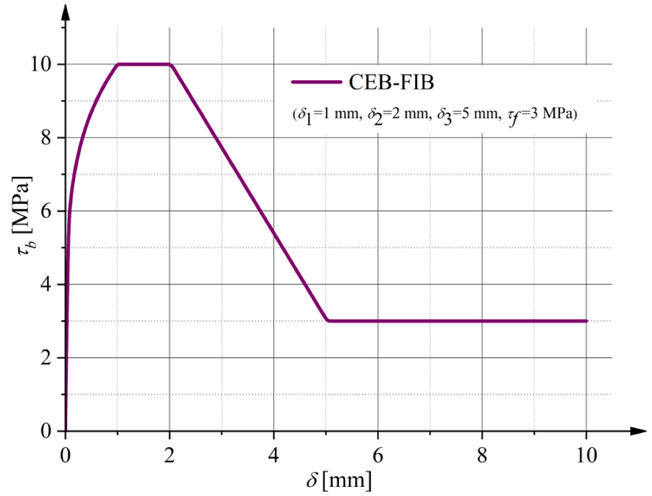

Fig. 8. Bond stress-slip relationship τ_b = f(δ) by CEB-FIP assumed in FE simulations.

for F_{max} = 802 kN. The beams S3D36A108_2 and S3D36A108_3 were damaged due to concrete crushing (C) in the constant bending moment zone for F_{max} = 601 kN and F_{max} = 954 kN (Table 2), respectively. Furthermore, the beams S3D36A108_2 and S3D36A108_3 (Fig. 3) had the relatively higher normalized deflection u/D and showed more ductility after reaching the peak load comparing to the beam S3D36A108_1. Note that beam S3D36A108_2 was made of weaker concrete. All deep beams S3D36A54 with η_a = 1.5 failed in shear-compression with a significant increase of the shear strength supported by an internal arch action (Fig. 4). The beam S3D36A54_2, which was made of weaker concrete, reached F_{max} = 1165 kN. For the other two beams the failure force was F_{max} = 1574 kN and F_{max} = 1271 kN respectively, (Table 2, Fig. 3a). The beams S3D36A54_1 and S3D36A54_3 had similar load–deflection curves that demonstrated a very stiff beam response connected with the high vertical load and small deflection. In contrast, the beam S3D36A54_2 due to weaker concrete possessed a relatively low ultimate force and large deflection (Fig. 3a). The post-peak behaviour was brittle (all beams lost their carrying capacity in a sudden failure).

2.2.2. RC beams of series '4': Varying effective beam depth D (ρ_l = 4.3% and ρ_l = 3.5%, ρ_s = 0.4%)

Similar to series '3', for series '4' it was observed that η_a had a great effect on the beam strength, brittleness and its failure mode [22]. The lowest beams S4D22A108 with η_a = 5.0 failed due to concrete crushing (CC) in the constant bending moment zone (Fig. 5), similarly to the beams with η_a = 6.0 in the series '3'. The average ultimate vertical force for the lowest beams was 207.3 kN (Table 2). The load–displacement curves (Fig. 3b) had similar shapes and pronounced post-peak structural softening. For the medium–high beams η_a = 2.5, two beams failed in the shear-compression (SC) with the F_{max} = 694 kN and F_{max} = 806 kN for S4D43A108_1 and S4D43A108_2 respectively. However, the beam S4D36A108_3 failed due to concrete crushing (CC) in the constant bending moment zone (Fig. 4b) at F_{max} = 732 kN (Table 2). The force–deflection curves (Fig. 3b) had similar shapes up to the peak load but later the post-peak behaviour was different. The beams S4D36A108_1 and S4D36A108_2 failed in a brittle way and the beam S4D36A108_3 in a quasi-brittle way. The highest beams S4D72A108 with η_a = 1.5 were first designed as prismatic beams with the rectangular cross-section ('trial beams'). The highest 'trial' beams denoted as S4D72A108_T1 and S4D72A108_T2 failed due to local concrete crushing at the supporting plate for F_{max} = 1375 kN. The third trial beam S4D72A108_T3 was strengthened by increasing its thickness locally at supports thus, it failed due to shear-compression at F_{max} = 1423 kN. The beams S4D72A108_1 and S4D72A108_2 had, however, 4 symmetric pilasters at all loading/supporting points (Fig. 2). Those beams also failed in shear-compression for a similar load, i.e. F_{max} = 1418 kN. The entire force–deflection curves of the beams S4D72A108_1, S4D72A108_2 and S4D72A108_T3 (Fig. 3b) were of a similar shape.

2.2.3. RC beams of series '3' and '4' as compared to previous tests by authors [20]

Fig. 6 presents the comparative results from current and previous

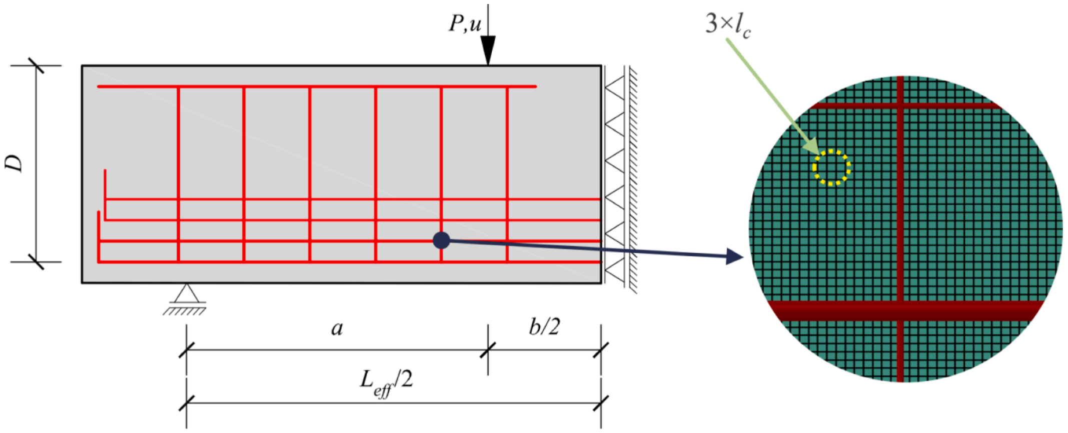

Fig. 9. Boundary conditions and FE mesh for RC beams (diameter of yellow circle is related to influence range of non-locality equal to 3 × l_c). (For interpretation of the references to colour in this figure legend, the reader is referred to the web version of this article.)

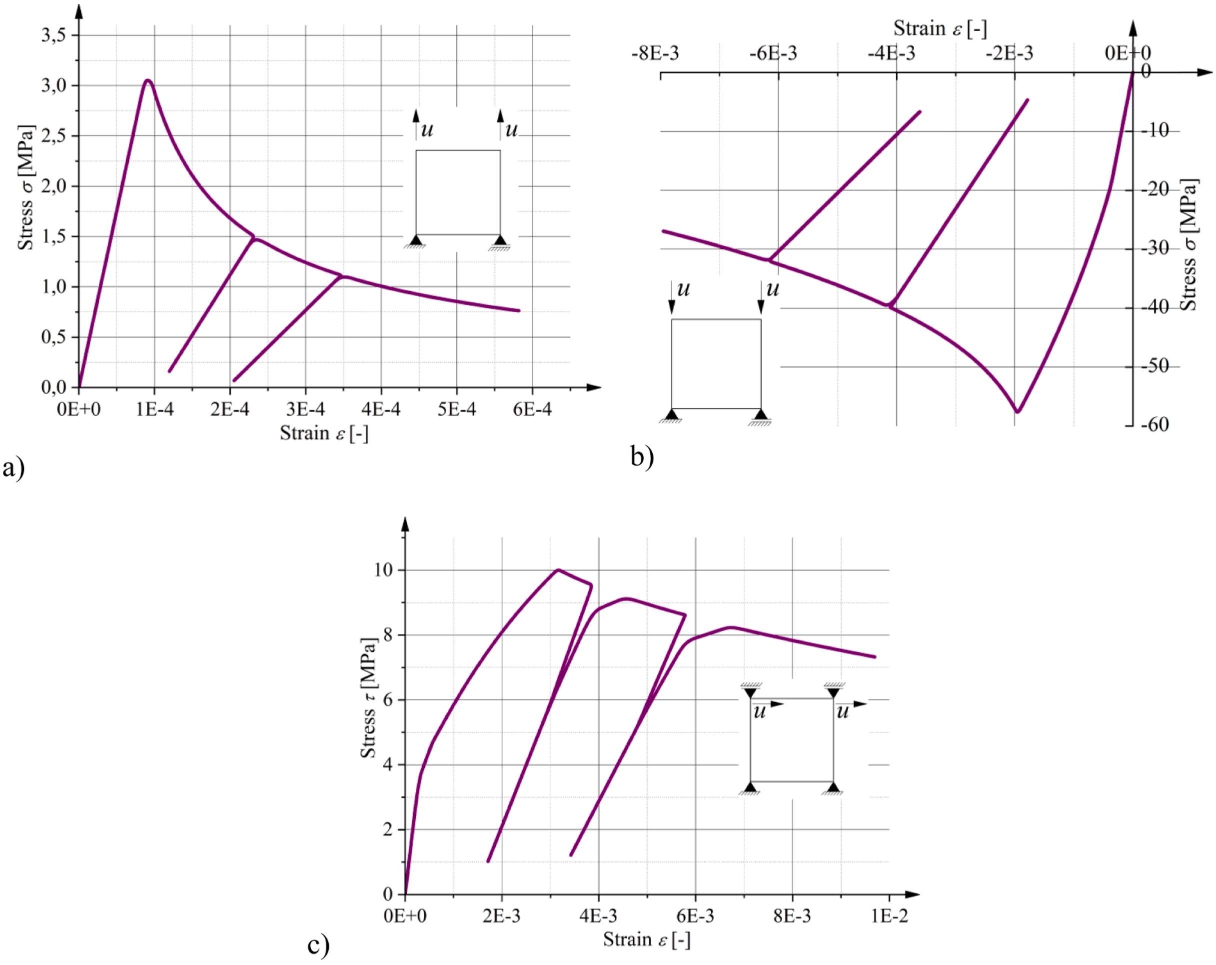

Fig. 10. Stress–strain curves for concrete from element tests using local elasto-plastic-damage model. a) cyclic uniaxial compression, b) cyclic uniaxial tension and c) cyclic simple shear.

experiments on the RC beams without shear reinforcement [20,22]. The RC beams with shear reinforcement in series '4' had higher strength than those in series '1' (Fig. 6a), in particular for the lower parameter η_a (up to 300% for $\eta_a = 1.5$). The presence of stirrups and a higher longitudinal reinforcement ratio also changed the failure mode. The slender beams with $\eta_a = 6$ without stirrups failed due to steel yielding in contrast to beams with stirrups for $\eta_a = 5$ that failed due to concrete crushing. The beams of transitional geometry for $\eta_a = 2.5$ without stirrups failed in diagonal tension mode whereas the beams with stirrups for $\eta_a = 3.0$ failed due to shear-compression/concrete crushing. The deep beams with $\eta_a = 1.0$–1.5 regardless of stirrups behaved similarly and failed under shear-compression conditions. In the beams without (series '2') and with stirrups (series '3'), a similar trend referring to the beam strength dependence on η_a was obtained when the parameter $\eta_a \leq 3$ (Fig. 6b). The ultimate shear stress did not change proportionally with η_a. The most pronounced increase of the ultimate shear stress was observed for $\eta_a = 1$ as compared to $\eta_a = 2$ in the series '2' [20]. The presence of the shear reinforcement in the beams with the varying shear span had a similar effect as in the beams with varying depth. The stirrups in the beams with $\eta_a = 3$ changed the failure mode from diagonal tension (series '2') into shear-compression/concrete crushing (series '3').

2.3. Transitional failure modes in experiments

The changes of the failure mode with the varying geometry parameter η_a and reinforcement ratios ρ_l and $\rho_{s.}$ are shown schematically in Fig. 7. The slender beams with the high η_a and without shear reinforcement failed due to steel yielding (symbol 'Y'). With decreasing parameter η_a, the failure mode changed from diagonal tension (symbol 'DT') for beams with a transitional geometry η_a to shear-compression (symbol 'SC') for deep beams . When the main reinforcement ratio increased (the steel yielding was eliminated), the slender beams failed in diagonal tension and the beams of a transitional geometry were damaged by either diagonal tension or shear-compression failure while the deep beams influenced by an arch action failed in shear-compression . Adding a sufficient amount of shear reinforcement ρ_s in slender beams (to suppress a shear failure mode) contributed to concrete crushing (symbol 'CC') in a constant bending moment zone . The 'CC' failure occurred before the main and shear reinforcement strength was achieved. The beams of a transitional geometry with shear reinforcement were damaged due to shear-compression or concrete crushing. The further increase of the shear reinforcement ratio might change the failure mode in deep beams from shear-compression to the damage of the support zone . The support zone failure in deep beams (symbol 'N') was due to insufficient nodal zone strength which was weaker than both the strut and tie strength.

3. FE modelling of concrete, reinforcement and bond-slip

3.1. Concrete

Different pure damage (e.g. [24–26]) and coupled elasto-plastic damage formulations (e.g. [27–34]) are used for describing the concrete fracture behaviour under various loading conditions,. The

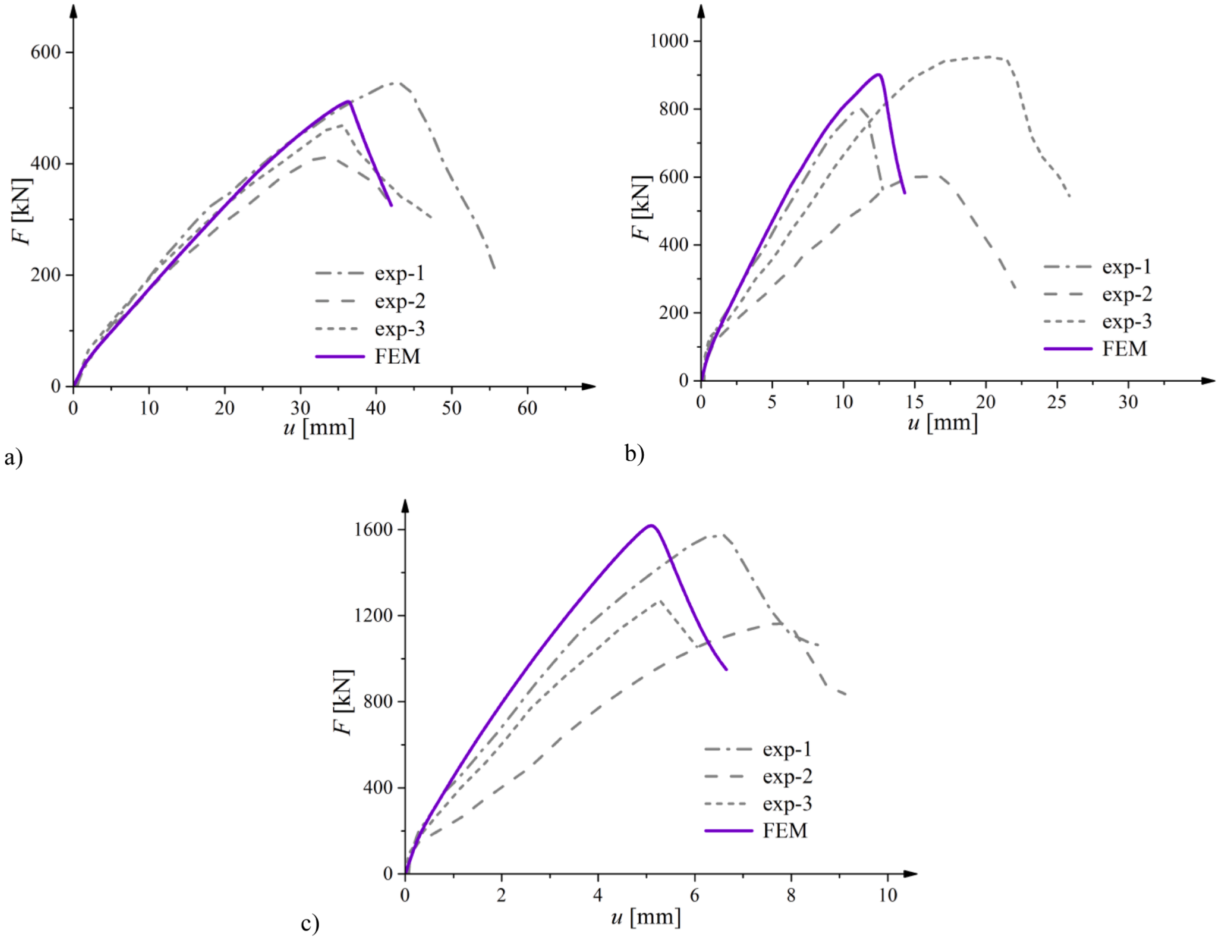

Fig. 11. Experimental [22] and calculated force–deflection $F = f(u)$ diagrams for RC beams of series '3' ($\rho_l = 4.3\%$): a) S3D36A216 ($\eta_a = 6$), b) S3D36A108 ($\eta_a = 3.0$) and c) S3D36A54 ($\eta_a = 1.5$).

Table 4
Failure vertical force F in experiments [22] and FE simulations (CC - concrete crushing in compressive zone, SC - shear-compression failure).

Beam type	Failure mode	Mean failure vertical force F (experiments) [kN]	Failure vertical force F (FEM) [kN]	Difference between FEM and experiments [%]
Series 3 S3D36A216 ($\eta_a = 6$)	CC CC CC	473.7	511.7	+8.0
Series 3 S3D36A108 ($\eta_a = 3$)	SC CC CC	878.0*	902.4	+2.8
Series 3 S3D36A54 ($\eta_a = 1.5$)	SC SC SC	1422.0*	1623.9	+14.2
Series 4 S4D22A108 ($\eta_a = 5$)	CC CC CC	207.3	213.8	+3.1
Series 4 S4D43A108 ($\eta_a = 2.5$)	SC SC CC	744	797.7	+7.2
Series 4 S4D72A108 ($\eta_a = 1.5$)	SC SC	1418.5	1546.6	+9.0

*Average value without beam made of weaker concrete.

formulations present a simplified isotropic (e.g. [24–26]) or a more realistic anisotropic damage concept (e.g. [27,28,30,31,34]).

The coupled isotropic elasto-plastic-damage approach formulated by the authors for concrete under monotonic and cyclic loading combines isotropic elasto-plasticity with scalar isotropic damage with the aid of a strain equivalence hypothesis [35,36]. Two variables control the damage growth in tension and compression for simulating crack closing and crack re-opening effects [21]. The constitutive model was successfully used in investigations of RC concrete beams under mixed shear-tension failure [37,62], composite RC-EPS slabs and walls under shear failure [38,39], and RC tanks under positive bending moments [40]. The direction of localized shear zones was realistically reproduced in simulations (due to the presence of plasticity in the constitutive formulation) despite the assumption of a simplified isotropic damage response in cracking. The performance of the constitutive formulation was also compared with other continuum constitutive laws including isotropic softening [41]. The constitutive model was described in detail in [21] and [40]. However, for the sake of paper clarity, the most important equations of the approach were listed below. Elasto-plasticity was defined in the effective stress space

$$\sigma_{ij}^{eff} = C_{ijkl}^{e}\varepsilon_{kl}.$$

A linear isotropic Drucker-Prager criterion with a non-associated flow rule in compression and a Rankine criterion with an associated flow rule in tension defined by the effective stresses were used within elasto-plasticity

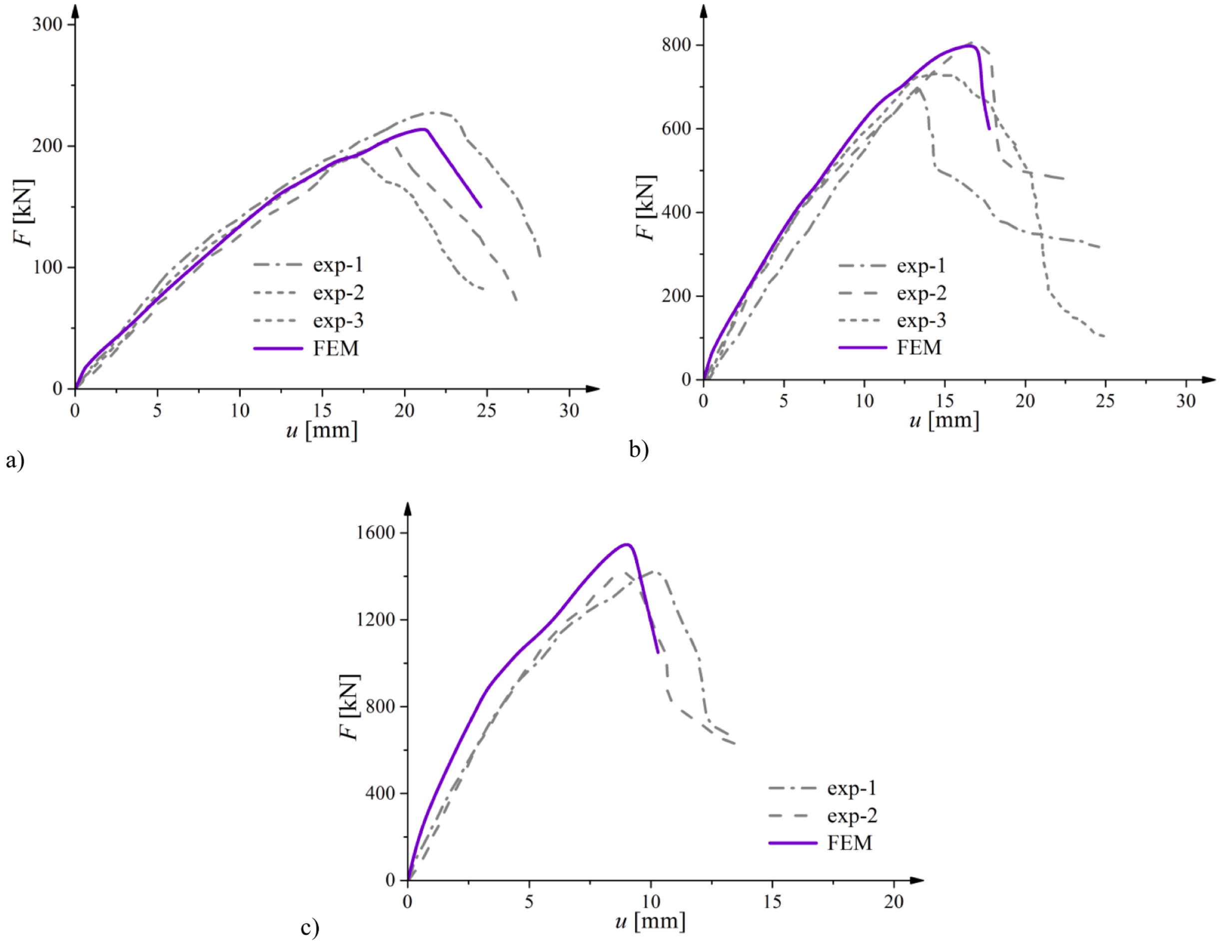

Fig. 12. Experimental [22] and calculated force–deflection $F = \mathrm{f}(u)$ diagrams for RC beams of series '4' ($\rho_l = 3.5\%$ and $\rho_l = 4.3\%$): a) S4D22A108 ($\eta_a = 5.0$), b) S4D43A108 ($\eta_a = 2.5$) and c) S4D72A108 ($\eta_a = 1.5$).

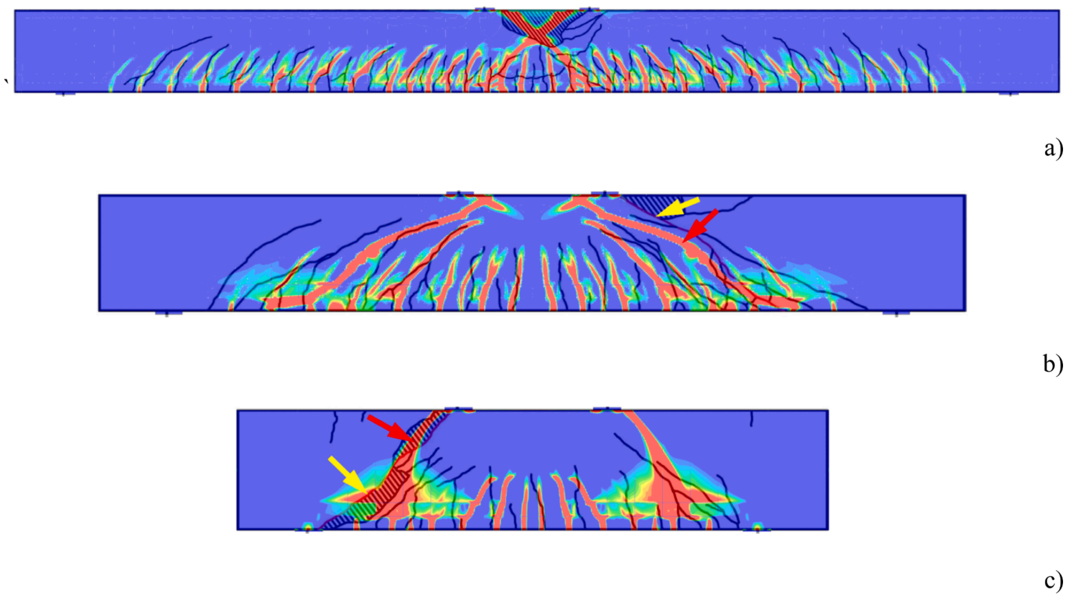

Fig. 13. Contours of non-local equivalent strain measure $\bar{\varepsilon}$ as compared with experimental crack pattern for RC beams of series '3' ($\rho_l = 4.3\%$): a) S3D36A216 ($\eta_a = 6.0$), b) S3D36A108 ($\eta_a = 3.0$) and c) S3D36A54 ($\eta_a = 1.5$) (experimental critical diagonal crack is marked by yellow arrow, numerical critical localization zone is marked by red arrow, note that beams are not proportionally scaled and steel bars are not shown). (For interpretation of the references to colour in this figure legend, the reader is referred to the web version of this article.)

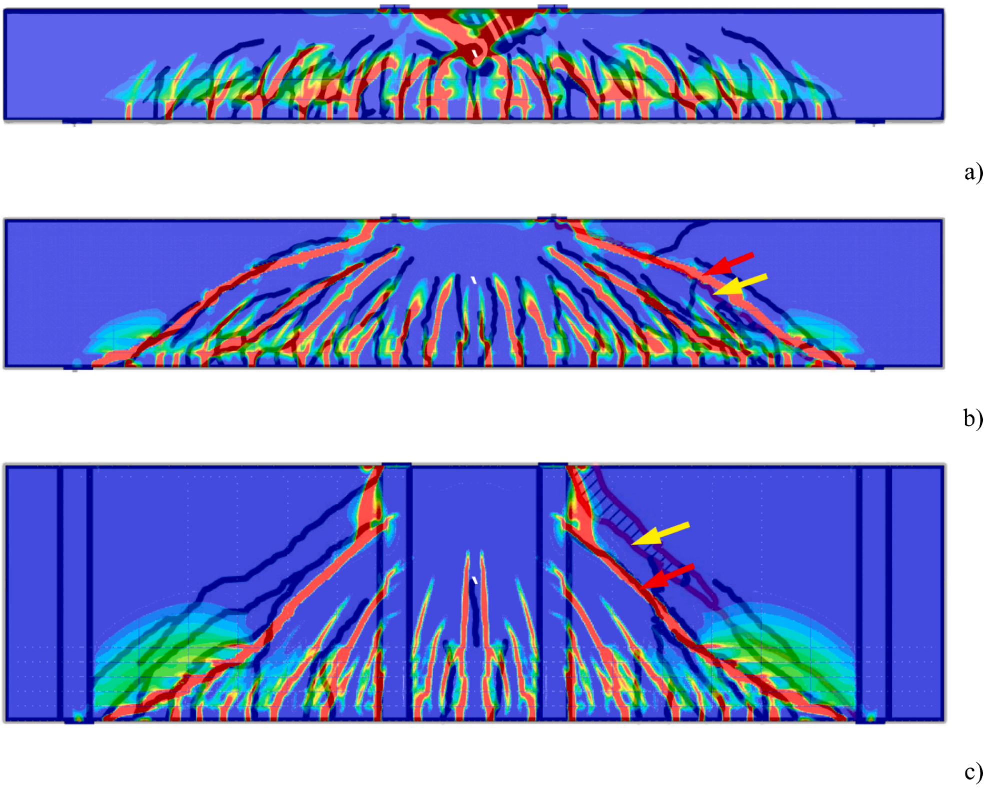

Fig. 14. Contours of non-local equivalent strain measure $\bar{\varepsilon}$ as compared with experimental cracks pattern for beams of series '4' ($\rho_l = 3.5\%$ and $\rho_l = 4.3\%$): a) S4D22A108 ($\eta_a = 5.0$), b) S4D43A108 ($\eta_a = 2.5$) and c) S4D72A108 ($\eta_a = 1.5$) (experimental critical diagonal crack is marked by yellow arrow, numerical critical diagonal localization zone is marked by red arrow, note that beams are not proportionally scaled and steel bars are not shown). (For interpretation of the references to colour in this figure legend, the reader is referred to the web version of this article.)

Table 5
Spacing of cracks in experiments [22] and localization zones in FEM simulations (CC - concrete crushing in compressive zone, SC - shear-compression failure).

Beam type	Failure mode CC or SC	Average spacing of cracks in experiments [mm]	Distance of localization zones in FE analyses [mm]
Series 3 S3D36A216 ($\eta_a = 6$)	CC	98	91
Series 3 S3D36A108 ($\eta_a = 3$)	CC/SC	114	100–110
Series 3 S3D36A54 ($\eta_a = 1.5$)	SC	110	98–127
Series 4 S4D22A108 ($\eta_a = 5$)	CC	79	84–91
Series 4 S4D43A108 ($\eta_a = 2.5$)	CC/SC	118	109–120
Series 4 S4D72A108 ($\eta_a = 1.5$)	SC	124	121–170

$$f_1 = q + p\tan\varphi - \left(1 - \frac{1}{3}\tan\varphi\right)\sigma_c(\kappa_1),$$

$$f_2 = \max\{\sigma_1, \sigma_2, \sigma_3\} - \sigma_t(\kappa_2),$$

$$g_1 = q + p\tan\psi,$$

where q is the Mises equivalent deviatoric stress, p - the mean stress, φ - the internal friction angle, $\sigma_c(\kappa_1)$ - the uniaxial compression yield stress, κ_1 – the hardening/softening parameter, σ_i – the principal stress, $\sigma_t(\kappa_2)$ – the tensile yield stress and κ_2 – the hardening/softening parameter equal to the maximum principal plastic strain ε_1^p, g_1 - the flow potential and ψ - the dilatancy angle ($\psi \neq \varphi$). The development of plasticity is governed by standard Kuhn-Tucker conditions.

The material degradation was calculated within isotropic damage mechanics, independently in tension and compression using one equivalent strain measure $\tilde{\varepsilon}$ by Mazars (ε_i - principal strains), defined in terms of total strains [25]

$$\tilde{\varepsilon} = \sqrt{\sum_i \langle \varepsilon_i \rangle^2}\ . \tag{5}$$

The stress–strain relationship was represented by the following formula

$$\sigma_{ij} = (1 - D)\sigma_{ij}^{eff}, \tag{6}$$

where

$$(1 - D) = (1 - s_c D_t)(1 - s_t D_c), \tag{7}$$

$$D_t = 1 - \frac{\kappa_0}{\kappa_t}\left(1 - \alpha + \alpha e^{-\beta(\kappa_t - \kappa_0)}\right), \tag{8}$$

$$D_c = 1 - \left(1 - \frac{\kappa_0}{\kappa_c}\right)\left(0.01\frac{\kappa_0}{\kappa_c}\right)^{\eta_1} - \left(\frac{\kappa_0}{\kappa_c}\right)^{\eta_2} e^{-\delta_c(\kappa_c - \kappa_0)}, \tag{9}$$

$$s_t = 1 - a_t\omega\left(\sigma_{ij}^{eff}\right) \text{ and } s_c = 1 - a_c\left(1 - \omega\ \left(\sigma_{ij}^{eff}\right)\right), \tag{10}$$

$$\kappa_t = \kappa\omega\left(\sigma_{ij}^{eff}\right) \text{ and } \kappa_c = \kappa\left(1 - \omega\left(\sigma_{ij}^{eff}\right)\right), \tag{11}$$

$$\omega\left(\sigma_{ij}^{eff}\right) = \begin{cases} 0 & \text{if } \sigma_i^{eff} = 0 \\ \dfrac{\sum\langle\sigma_i^{eff}\rangle}{\sum|\sigma_i^{eff}|} & \text{otherwise.} \end{cases} \tag{12}$$

The variable κ is the maximum equivalent strain attained in the loading history

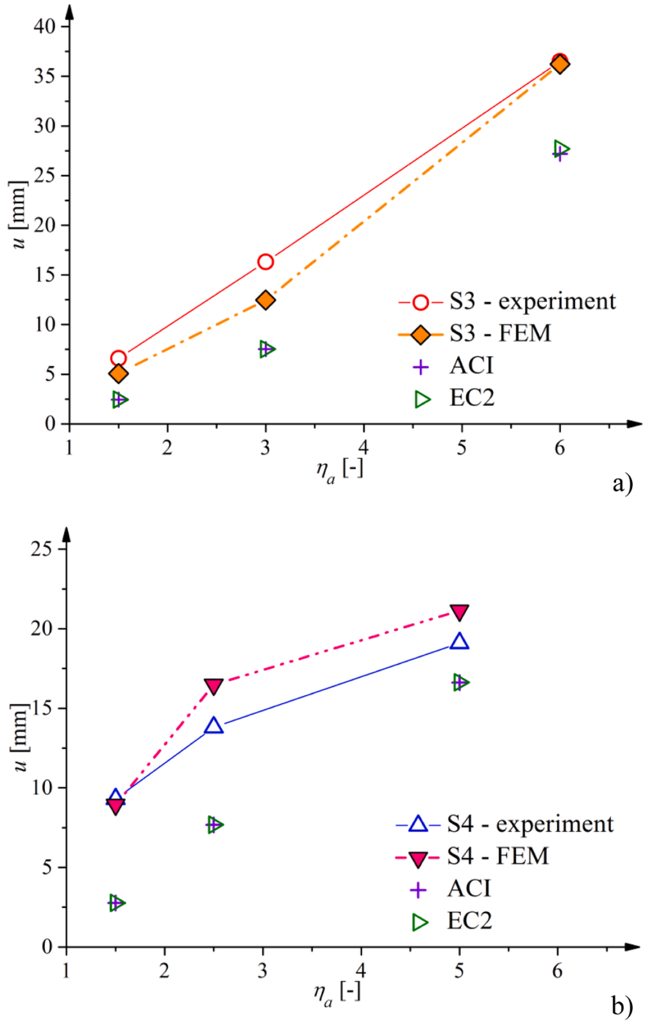

Fig. 15. Beam deflections u according to FE-calculations and analytical formula from EC2 and ACI versus η_a for $F_{\max}$ as compared to experiments [22]: a) series '3' (S3) and b) series '4' (S4).

$$\kappa(t) = \max_{\tau \leq t} \widetilde{\varepsilon}(\tau). \tag{13}$$

The damage initiation and growth is described by the Kuhn-Tucker conditions:

$$f \leq 0, \dot{\kappa} \geq 0, \dot{\kappa} f = 0, \tag{14}$$

where

$$f = \widetilde{\varepsilon} - \kappa. \tag{15}$$

The tensile and compressive damage functions D_t and D_c consider the damage evolution under tension [42] and compression [43] by the following material constants: α, β, η_1, η_2 and δ_c. The damage under tension was here separately controlled in FE simulations by the threshold parameter κ_t and the damage under compression by the threshold parameter κ_c. In the case of a linear hardening model, the following 16 material constants are required: E, υ, κ_0, α, β, η_1, η_2, δ_c, a_t, a_c, φ, ψ, initial yield stresses σ^0_{yt} (tension) and σ^0_{yc} (compression) and plastic hardening moduli H_p (in compression and tension) (Table 3). The constitutive law is similar to the model by Lee and Fenves [44] that was proved to not violate thermodynamic principles (lack of the spurious energy dissipation) [45]. The constitutive law consists of two main steps. First, the elasto-plastic strain rate decomposition is performed in the effective stress space, described by a combination of both the Drucker-Prager and Rankine criteria. Second, the damage is introduced; the equivalent strain measure (Eq.5) is calculated concerning a strain decomposition from the first stage (assuming the strain equivalence hypothesis [36]). Next, the material degradation is separately computed in tension and in compression (Eqs.8 and 9). Finally, the total stress is updated (Eq.6) with the component (1-D) by Eq.7. Two independent simple monotonic tests (uniaxial compression and uniaxial tension or three-point bending) for the already fixed damage splitting factors a_t and a_c can be used for calibration purposes [21].

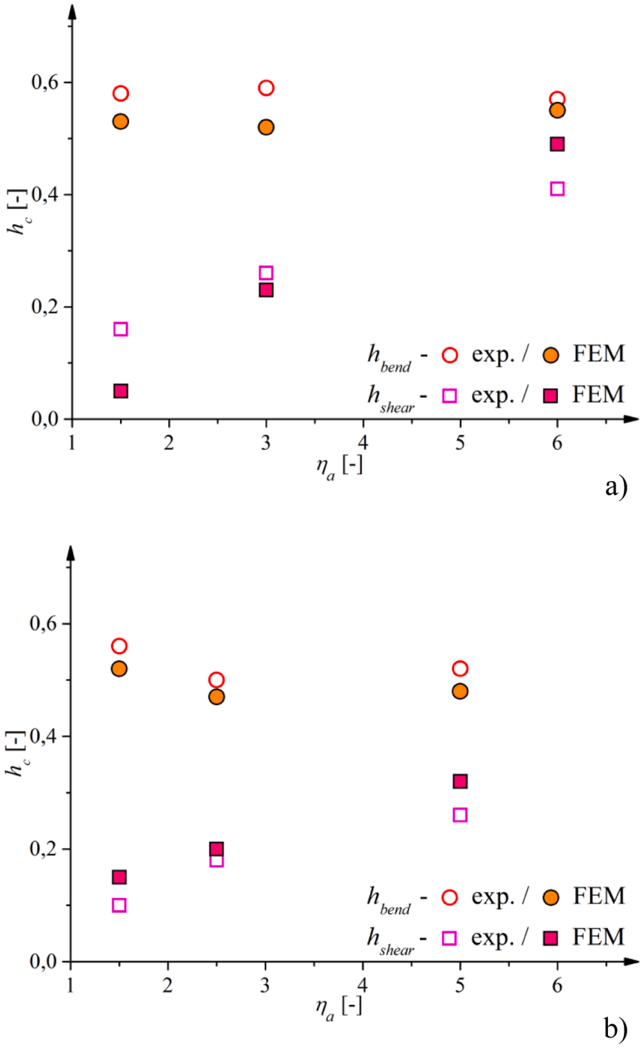

Fig. 16. Average normalized calculated compressive zone height h_c/D as compared to measure values [22] in RC beams of series '3' (a) and beams of series '4' (b).

For properly reproducing strain localization and to capture a deterministic size effect (dependence of the nominal strength on the structure size) [46–49], an integral-type non-local theory was used as a regularization technique that does not violate thermodynamic principles [50]. The damage part was solely made non-local since the elasto-plastic part of the model produced no softening. It was modified in softening by replacing the local equivalent strain measures with its non-local counterpart according to the formula

$$\overline{\varepsilon}(\boldsymbol{x}) = \frac{\int_V w(\|\boldsymbol{x} - \boldsymbol{\xi}\|)\widetilde{\varepsilon}(\boldsymbol{\xi})d\boldsymbol{\xi}}{\int_V w(\|\boldsymbol{x} - \boldsymbol{\xi}\|)d\boldsymbol{\xi}} \tag{16}$$

where $\boldsymbol{x}$ – a considered point and $\boldsymbol{\xi}$ – neighbour points. As a weighting function $\boldsymbol{w}$ Gauss distribution function was used

Table 6
Experimental and theoretical shear strengths/ultimate stresses according to various analytical models of Section 4 (ν_C^{Exp} – experimental average shear stress of beams failing due to concrete crushing, ν_{SC}^{Exp} – experimental average shear strength of beams failing due to shear-compression, C - concrete crushing in compressive zone, SC - shear-compression failure) [22].

Beam	η_a	Failure mode	ν_C^{Exp}	ν_{SC}^{Exp}	ν^{EC} (Eqs. A1/A2)	ν^{Fl} (Eq. A12)	ν^{STM} (Eq. A4)	ν^{MSTM} (Eq. A7)	ν^{CSTM} (Eq. A9/A10)
S3D36A216	6	C	2.64	–	2.03	2.86	–	–	–
S3D36A108	3	C/SC	5.30	4.46	2.03	5.72	4.52	5.91	3.63
S3D36A54	1.5	SC	–	7.90	2.03	–	8.22	10.43	8.43
S4D22A108	5	C	3.14	–	2.11	3.38	–	–	–
S4D43A108	2.5	C/SC	5.67	5.82	2.11	6.84	4.97	6.78	4.65
S4D72A108	1.5	SC	–	6.52	2.11	–	6.83	10.11	5.19

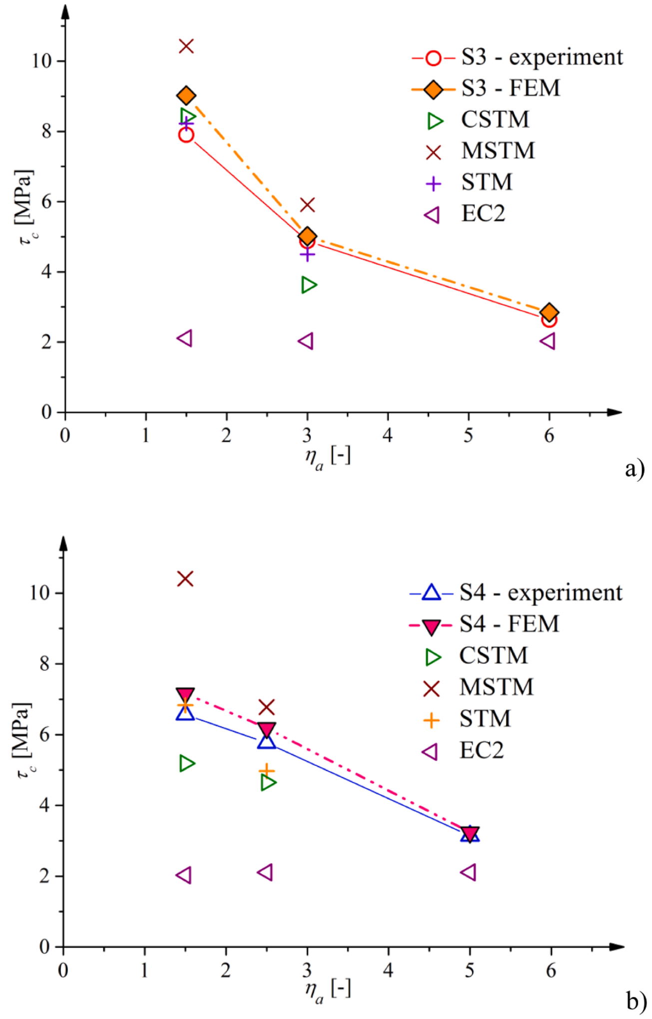

Fig. 17. Average experimental ultimate shear strength τ_c [22] as compared to FE calculations and analytical solutions based on STM, MSTM, CSTM and EC2 for: a) RC beams of series '3' and b) RC beams of series '4' (b) (note that STM and MSM are valid for $\eta_a \leq 2$ and CSTM for $\eta_a \leq 2.5$).

$$w(r) = \frac{1}{l_c\sqrt{\pi}} \exp\left(-\left(\frac{r}{l_c}\right)^2\right) \tag{17}$$

where l_c denotes the characteristic length of the microstructure. The averaging is restricted to the small area around the considered point (the influence of neighbor points at the distance of $3 \times l_c$ is only 0.01%). The function in Eq.17 satisfies the normalizing condition [47]. The numerical results indicate that the greater l_c, the higher are both the strength and ductility of elements [51]. An inverse identification process of experimental data is usually used to determine a characteristic length l_c [52,53]. The characteristic length l_c of micro-structure, assumed for concrete within isotropic elasto-plasticity and isotropic damage mechanics as about l_c = 1.2–1.5 mm. To obtain mesh-independent results, the element mesh size s_e should be smaller or equal to $s_e \leq 2 \times l_c$ [51]. The calculations with l_c = 1.2–1.5 mm lengthen the computation time without an insignificant effect on the results [40]. We assumed l_c = 2 mm in the FE analyses as in [21,40]. The FE results with l_c = 2 mm were proved to be mesh-objective [40]. The important effect of non-linearity in the compressive region which counteracts a shortcoming of the constitutive model caused by an isotropic response in cracking was discussed in detail in [21]. On the other hand, the calculations within pure elasto-plasticity with a failure surface described by Drucker-Prager and Rankine criteria provided an unrealistic solution for the shear-compression failure in RC beams [41].

3.2. Reinforcement and bond-slip law

For simulating the behaviour of steel bars, an elastic-perfectly plastic constitutive model was assumed with the modulus of elasticity of E_s and yield stress σ_y. All longitudinal and transverse bars were modelled as one-dimensional truss elements. For describing the interaction between concrete and reinforcement, a bond-slip law was defined for longitudinal bars only. The interface with a zero thickness was chosen along a contact line where a relationship between the shear traction and slip was introduced. The contact elements may be, thus, treated as cohesive elements with a law defined in a tangential direction. In the current paper, a bond-slip law after CEB-FIB code [54] was assumed, thus the relationship between the bond shear stress and slip was as follows (Fig. 8):

$$\tau_b = \begin{cases} \tau_{max}\left(\dfrac{\delta}{\delta_1}\right)^{\alpha} & 0 < \delta \leq \delta_1 \\ \tau_{max} & \delta_1 < \delta \leq \delta_2 \\ \tau_{max} - \left(\tau_{max} - \tau_f\right)\dfrac{\delta - \delta_1}{\delta_3 - \delta_2} & \delta_2 < \delta \leq \delta_3 \\ \tau_f & \delta_3 < \delta \end{cases} \tag{18}$$

This bond-slip law describes 4 different phases by taking hardening/softening into account in the relationship. We assumed the following bond values in FE simulations: $\tau_{\max}$ = 10 MPa, τ_f = 3 MPa, δ_1 = 1 mm, δ_2 = 2 mm, δ_3 = 5 mm and α = 0.2 [21], based on pull-out tests in the concrete block with steel bars of the diameter ϕ = 12 mm [14,55] (the pull-out tests with steel bars of ϕ = 20 mm were not carried out). Since the calculated bond stresses τ_b were clearly below $\tau_{\max}$, the effect of ϕ on $\tau_{\max}$ was neglected. The perfect bond was adopted between concrete and stirrups.

The constitutive model for concrete was implemented into the commercial finite element code Abaqus Standard [56]. To introduce the constitutive models for concrete and reinforcement, bond-slip law and non-local averaging, the user constitutive law definition (UMAT) and user element definition (UEL) subroutines were introduced (see the details in [40]).

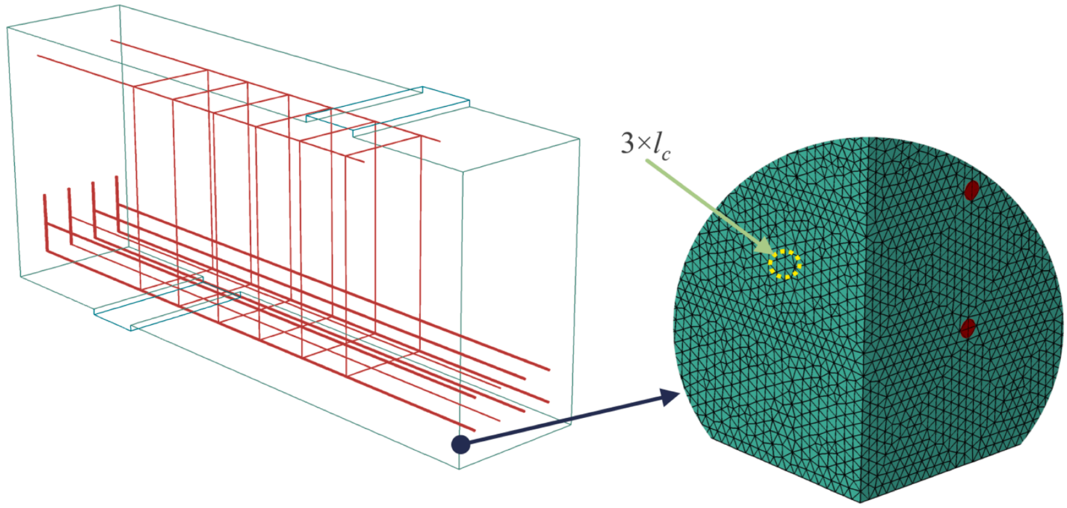

Fig. 18. Geometry of the 3D FEM model and an exemplary fragment of FE mesh for RC beam S3D36A54 ($\eta_a = 1.5$) (diameter of yellow circle is related to influence range of non-locality $3 \times l_c$). (For interpretation of the references to colour in this figure legend, the reader is referred to the web version of this article.)

4. FE analyses of experimental RC beams with stirrups

4.1. FE input data

The FE analyses were mainly conducted under plane stress conditions due to the small thickness of beams (as in [21]). Assuming out-of-plane stress components equal to zero was a natural choice for 2D numerical modelling. In addition, one full 3D calculation was also performed for the smallest beam (S3D36A54, $\eta_a = 1.5$) for comparison purposes. In the FE calculations, some further simplifications were assumed. First, the half part of beams was analyzed only (Fig. 9) to reduce the computation time (as in [21]). Thus, a symmetric failure mode was taken into account in contrast to the experimental results. The effect of a statistical distribution of the concrete tensile strength [57] on the location of the critical diagonal crack was also neglected. In the present 2D FE simulations, the meshes consisting of 72,500–224,200 plane stress four-node rectangular elements with selectively reduced integration were used to avoid locking (Fig. 9). The size of quadrilateral elements, $s_e = 2$ mm, was equal to $s_e = l_c = 2$ mm (Fig. 9).

The material constants (Table 3) were fitted to the experimental modulus of elasticity of $E = 34$ GPa, uniaxial compressive strength of concrete $f_c = 58$ MPa and experimental tensile strength of concrete cylinders during splitting tension $f_t = 3.2$ MPa (as in [21]. Due to the lack of laboratory full stress–strain curves during uniaxial compression and uniaxial tension, the tensile G_f and compressive fracture energy G_c were assumed, based on the literature data. Using the assumed material constants (Table 3), the tensile fracture energy was $G_f = 100$ N/m and compressive fracture energy $G_c = 4000$ N/m ($G_c/G_f = 40$). The calculated uniaxial compressive strength was $f_c = 58$ MPa, the uniaxial tensile strength was $f_t = 3.05$ MPa and the shear strength was $\tau_{max} = 10$ MPa ($\tau_{max} \approx \sqrt{f_c f_t}$) (Fig. 10). For reinforcement: the elastic modulus was $E_s = 200$ GPa and the yield stress was $f_y = 560$ MPa.

4.2. Numerical results and discussion

The calculated force–displacement curves for RC beams with stirrups were compared to the experiments in Fig. 11 (series '3')' and Fig. 12 (series '4'). The same failure mode occurred in experiments and numerical calculations. The experimental ultimate vertical forces were satisfactorily reproduced in the FE analyses. The difference between the numerical and experimental results was 3–14% for the RC beams of series '3' and 3–9% for the RC beams of series '4' (Table 4). The curve inclination in a hardening/softening phase was properly reflected. The discrepancies increased with decreasing parameter η_a.

Figs. 13 and 14 show the contours of the non-local equivalent strain measure $\bar{\varepsilon}$ as compared with the experimental crack pattern (marked as lines). For the sake of clarity, the longitudinal and transverse steel bars were not shown. The calculated strain localization zones were symmetric in contrast to the experimental cracks (Figs. 13 and 14). However, the overall characteristics of failure modes, i.e. concrete crushing (C) and shear-compression failure mechanism (SC) were correctly reproduced in the FE simulations. In general, the geometry of localized zones from FEM satisfactorily matched the experimental crack pattern (Figs. 13 and 14), although some differences existed, especially for the RC beams with the low parameter $\eta_a = 1.5$. For the RC beam S3D36A54 ($\eta_a = 1.5$), a too diffused shear localized zone was calculated in the shear-span region (Fig. 13c). For the RC beam S4D72A108 ($\eta_a = 1.5$), the inclination of the calculated critical localized zone was too low (by about 7°) (Fig. 14c). For the beam S3D36A108 ($\eta_a = 3.0$), the critical localized zone was located at a certain distance (0.17 m) from the right support (Fig. 13b) in contrast to the experiment wherein it was located at the right support. In general, the total number of localized zones in RC beams in FE simulations was slightly higher than in experiments (Fig. 14a). The average distance of all calculated localization zones (including main and secondary zones) along the beam span was smaller by about 2.4–12% as compared with the experimental average crack spacing (main and secondary cracks) (Table 5). The highest difference of 37% occurred for the RC beam S4D72a108 ($\eta_a = 1.5$) (Fig. 14c) when considering solely major localization zones propagating through all longitudinal rebar layers. For the RC beam S3D36A54 ($\eta_a = 1.5$) (Fig. 13c), the difference was 15.5% without considering a diffused shear localization zone.

As in the experiments, the calculated mid-length deflections of RC beams (measured at the beams' mid-span) increased with increasing η_a (Fig. 15). They were lower by 1.0–23.5% (series '3') and higher by 3.8–19.5% (series '4') than in the experiments. In addition, the beam deflections were calculated with the formulae by EC2 [58] and ACI [59] by neglecting creep. For all tested beams, the experimental mid-length deflections were underestimated by about 15–70% as compared to the design code formulae (Fig. 15).

The experimental mean normalized height of the compressive zone

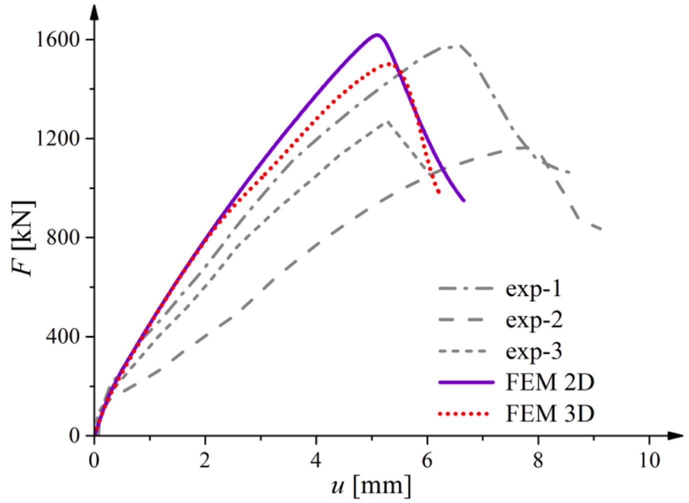

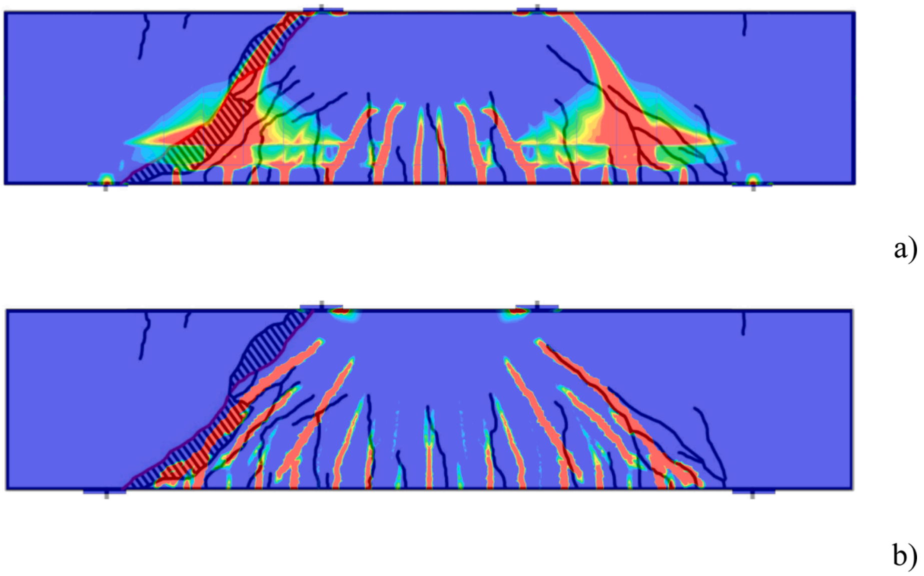

Fig. 19. Calculated force–deflection curves and distributions of non-local equivalent strain measure from FE analyses as compared to experiments (beam S3D36A54, $\eta_a = 1.5$) in: a) 2D and b) 3D FE simulations.

in the pure bending b and shear zone a against η_a prior to the failure [22] as compared to the numerical results is described in Fig. 16. The agreement between experimental and numerical results is good. The height of the calculated compressive zone in the pure bending part was nearly independent of η_a. The height of the calculated compressive zone in the shear span proportionally increased with increasing η_a. Similar trends were observed in experiments (Fig. 16).

5. Comparison of shear strength between experimental, numerical and analytical results

The experimental (Fig. 3) and numerical (Figs. 11 and 12) results of the shear strength of RC beams with stirrups were compared with the simplified analytical predictions used in engineering practice. The model based on the truss analogy in Eurocode [58], the strut-and-tie model (STM) in ACI [60], the modified strut-and-tie model (MSTM) proposed by Zhang and Tan [16] and the cracking strut-and-tie model (CSTM) derived by Chen et al. [61] were chosen. The models MSTM and CSTM were taken as an example. Note that all analytical formulae described in the literature consider a failure pattern in a simplified way and are not able to distinguish between two different failure modes in shear (diagonal tension and shear compression) which affect the beam strength to a different degree. The analytical formulae were described in Appendix. Table 6 includes the experimental and theoretical shear strengths/ultimate stresses according to the various analytical models.

Fig. 17 compares the experimental, numerical and analytical shear strengths $\tau_c = P_{\max}/(tD)$ (where $P_{\max} = 0.5F_{\max}$) for the RC beams of series '3' and '4'. For the beams of a transitional geometry (beam S3D36A108 with $\eta_a = 3.0$ and S4D43A108 with $\eta_a = 2.5$), the shear strength was calculated using both the beam theory and strut-and-tie models for $\eta_a = 1.5$, 2.5 and 3.0 (even though it is postulated that the parameter $\eta_a \leq 2.0$ in [60] and [16] and $\eta_a \leq 2.5$ in [61].

According to the simple strut-and-tie model (STM) from ACI 318–14 (Eq.A4) (valid for $\eta_a \leq 2.0$), the predicted shear strengths of deep beams

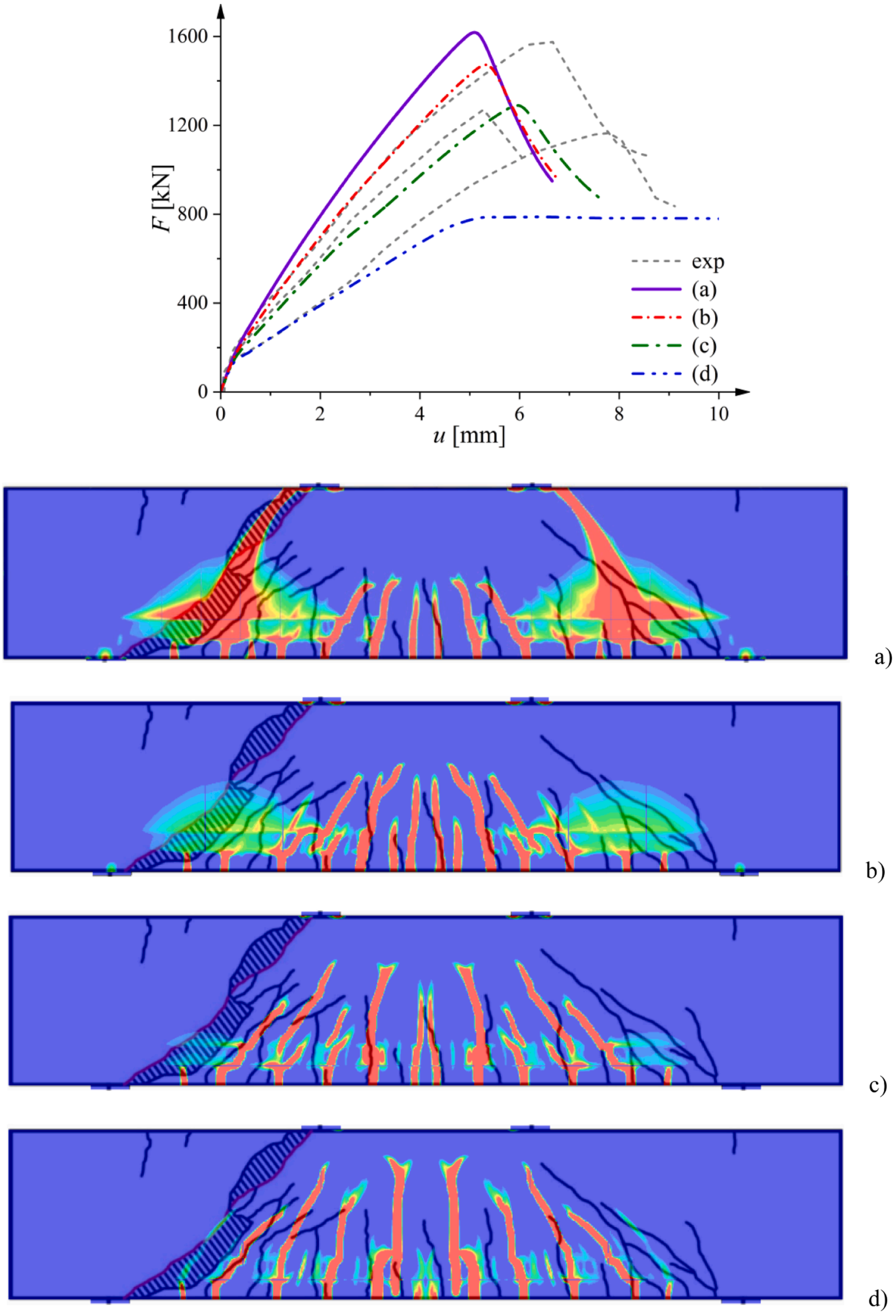

Fig. 20. Calculated force–deflection curves and distributions of non-local equivalent strain measure from FE analyses as compared to experiments (beam S3D36A54, $\eta_a = 1.5$) for different longitudinal reinforcement ratio: a) initial amount ($\rho_l = 4.3\%$), b) 0.75, c) 0.5, and d) 0.25 of initial amount.

with $\eta_a = 1.5$ were very close to experimental results in both the series '3' and '4' (higher solely by 5–10%) (Table 6 and Fig. 17). With respect to the beams with a transitional geometry, the predicted shear strength was the same as the experimentally obtained value for $\eta_a = 3$ with the shear-compression failure mode. The analytical solution provided for $\eta_a = 2.5$ (close to the application range) the lower shear strength by 15% as compared to the experimental beams that failed due to shear-compression (Fig. 17). The calculated beam strength resulting from the nodal zone strength was higher in all beams by 7% (CCT node) and 33% (CCC node) than the theoretical strut nominal strength (for the beam S4D72A108 the difference further increased up to 80% and 130% accordingly with the pilaster thickness of 250 mm). The measured ultimate vertical forces of beams with $\eta_a = 2.5$–3.0 were by 1–8% lower than estimated based on the CCT node strengths. In contrast, the high beams with $\eta_a = 1.5$ were stronger by 10–12% with respect to the theoretical beam strengths resulting from the CCT node failure.

Referring to the model by Zhang and Tan [16] (Eq.A7) (MSTM) (valid for $\eta_a \leq 2.0$), the calculated shear strengths of beams with η_a between 1.5 and 2.5 were generally higher than the experimental results: by 40%-55% ($a/D = 1.5$) and by 15% ($a/D = 2.5$). Note that MSTM was successfully verified by Zhang and Tan [16] against the deep beams with $\eta_a = 1.1$ that indicated this model had limited applicability. Based

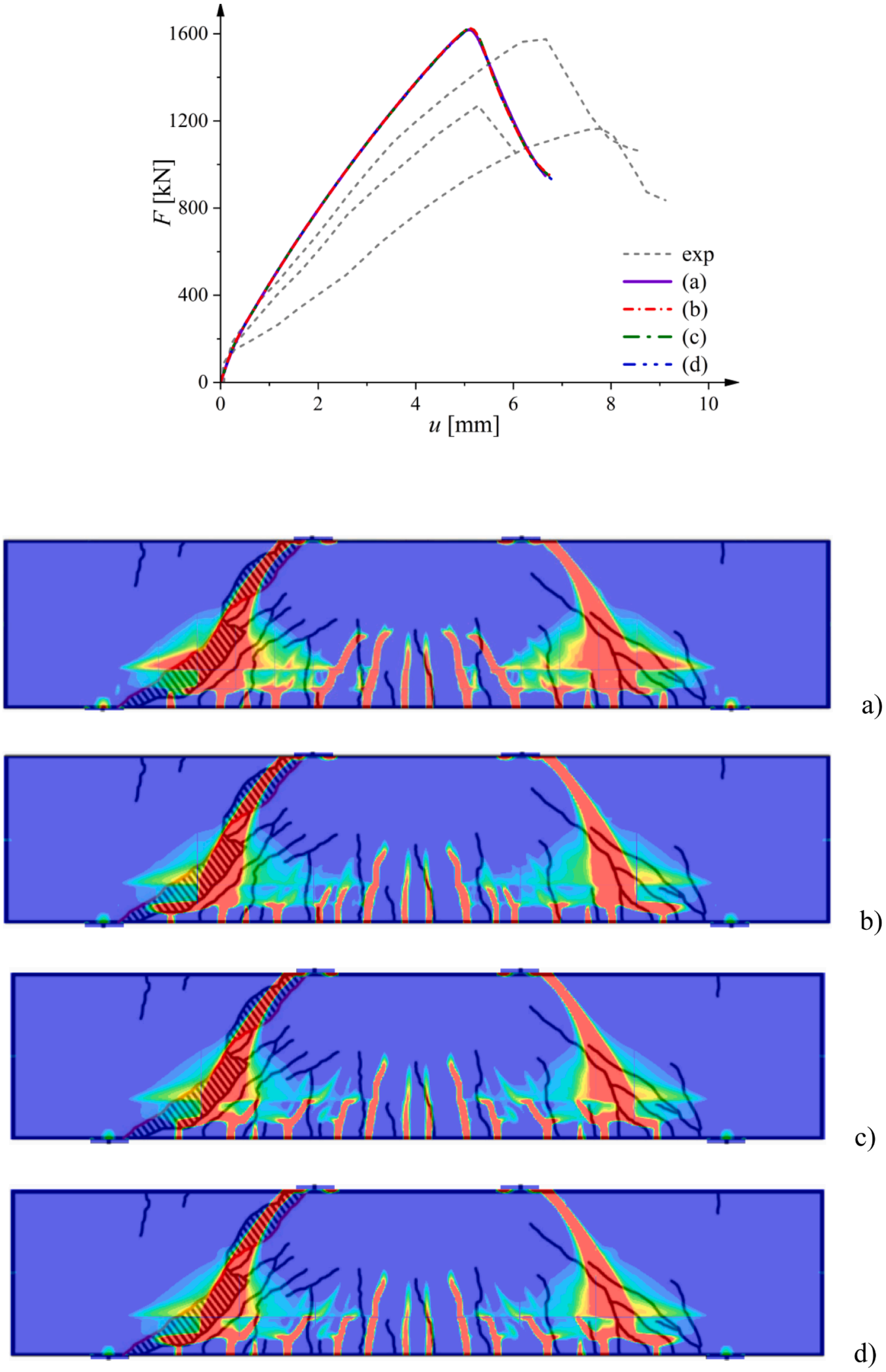

Fig. 21. Calculated force–deflection curves and distributions of non-local equivalent strain measure from 2D FE analyses as compared to experiments (beam S3D36A54, $\eta_a = 1.5$, $\rho_l = 4.3\%$) for different shear reinforcement ratio ρ_s: a) $\rho_s = 0.4\%$ (basic value), b) $0.75\rho_s$, c) $0.5\rho_s$, and d) $0.25\rho_{s.}$

on the cracking strut-and-tie model (CSTM) by Chen et.al. [61] (valid for $\eta_a \leq 2.5$), the estimated shear strength related to the experimental results $\nu^{\mathrm{STM}}/\nu^{\mathrm{Exp}}$ varied between 0.80 and 1.05 for the beams with $\eta_a = 1.5$ and was 0.80 with $\eta_a = 2.5$. The highest difference of 25% was obtained for the beam with $\eta_a = 3.0$ that was however beyond the model application range. The CSTM predicted the lowest ultimate shear strength (for $\eta_a \leq 3.0$) among all analyzed strut-and-tie models. The shear stresses of the beams with $\eta_a = 3.0$–6.0 failing due to concrete crushing were estimated with the 8%-error using a simple equilibrium condition of plane section. However, the beams' strength with $\eta_a = 2.5$ was overestimated by 20%. The formula recommended by EC2 [58] obviously strongly underestimated the ultimate shear strength of all beams failing in shear-compression (the difference was exceeded by 100% for $\eta_a =$ 2.5–3.0).

The theoretical strut width w_s was obviously 2.5–4 times wider than the experimental crack spacing s_l^{EXP} since, in an idealized truss model, a

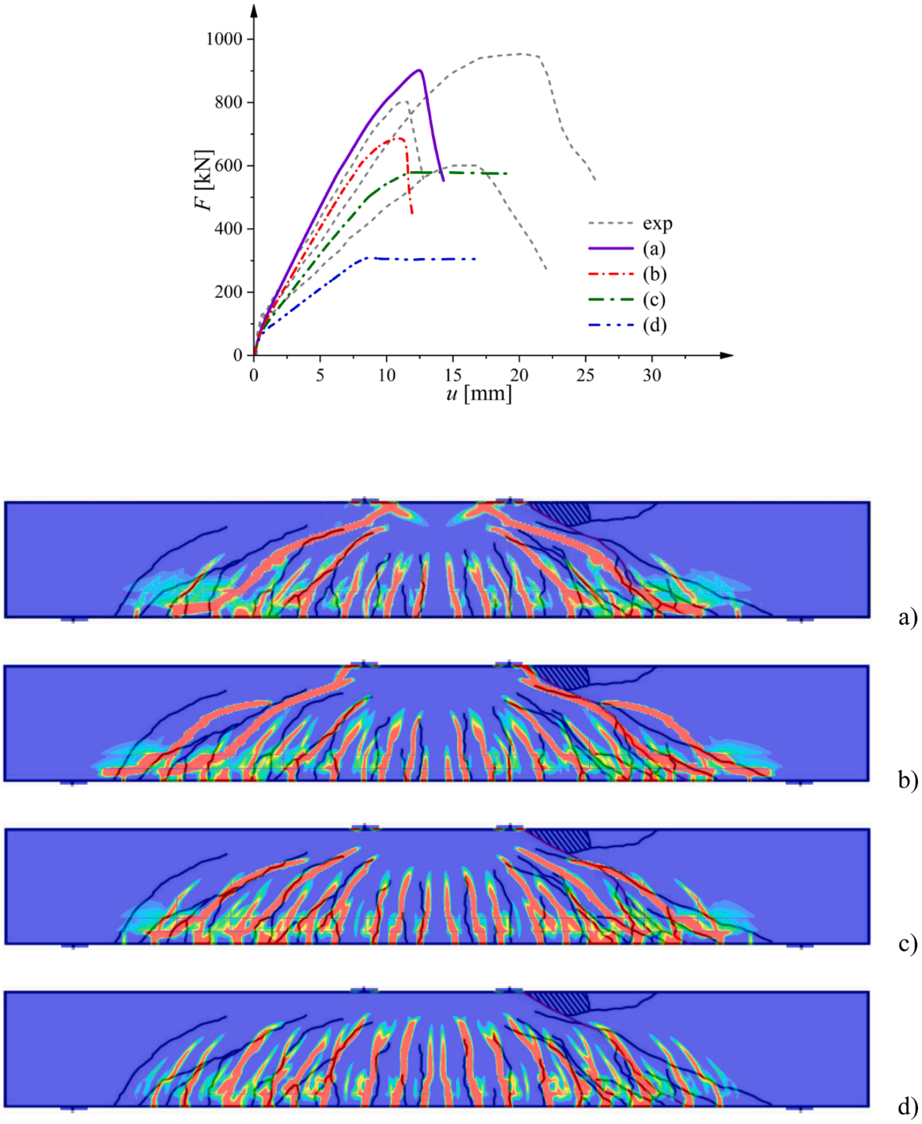

Fig. 22. Calculated force–deflection curves and distributions of non-local equivalent strain measure from 2D FE analyses as compared to experiments (beam S3D36A108, η_a = 3.0, ρ_s = 0.4%) for different longitudinal reinforcement ratio ρ_l: a) ρ_l = 4.3% (basic value), b) 0.75ρ_l, c) 0.5ρ_l, and d) 0.25ρ_L.

single strut represented several real struts between cracks. The theoretical inclination of the strut θ_s in STM [60] was always lower than the critical shear crack inclination $\theta_S{}^{EXP}$ by 20–50% for η_a = 2.5–3.0 and 10–25% for η_a = 1.5. MSTM [16] and CSTM [61] further reduced the strut inclination that were by 40–60% and 30–40% lower than the critical shear crack inclination for η_a = 2.5–3.0 and η_a = 1.5, respectively. This observation confirmed that the presented STMs should not be used for the beams with η_a = 2.5–3.0 due to an incorrect assumption of a single strut connecting a loading and bearing plate. In the case of beams with η_a = 1.5, the simple ACI model [60] provided an acceptable difference between the calculated strut inclination and critical shear crack inclination.

In summary, the best prediction of the shear strength was obtained with the simple strut-and-tie model following ACI [60] (5%-error for η_a = 1.5, 15%-error for η_a = 2.5 and 1%-error for η_a = 3.0). In the RC beams without stirrups [20], ACI [60] offered, however, very incorrect results for η_a = 1.5–2.0 (error of 20–100%) and realistic results for η_a = 1.0 (error of 5%). STMs were very sensitive to a different number of reinforcement layers. The increasing number of layers affected the height of the support nodal zone (CCT node), the strut width and its inclination. The more reinforcement layers, the higher was the beam strength even with the same reinforcement ratio. The discrepancies between the experimental and theoretical results were mainly caused by the varying strut widths and strut inclinations for all high beams for η_a = 1–2 and the different shapes of compressive struts in beams with η_a = 2.

The numerical effect of different material constants of concrete and bond-law stiffness on FE results was shown for RC beams without shear reinforcement [21]. The numerical shear strength of RC beams became higher with increasing tensile and compressive fracture energy, tensile and compressive strength and slip-bond stiffness. During the diagonal tension failure, the effect of tensile parameters was stronger and during shear compression failure, the effect of compressive parameters was more pronounced.

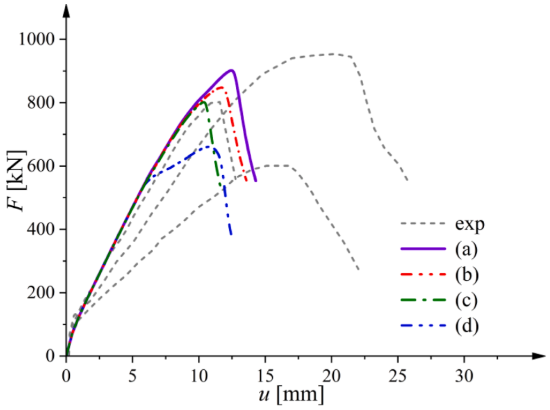

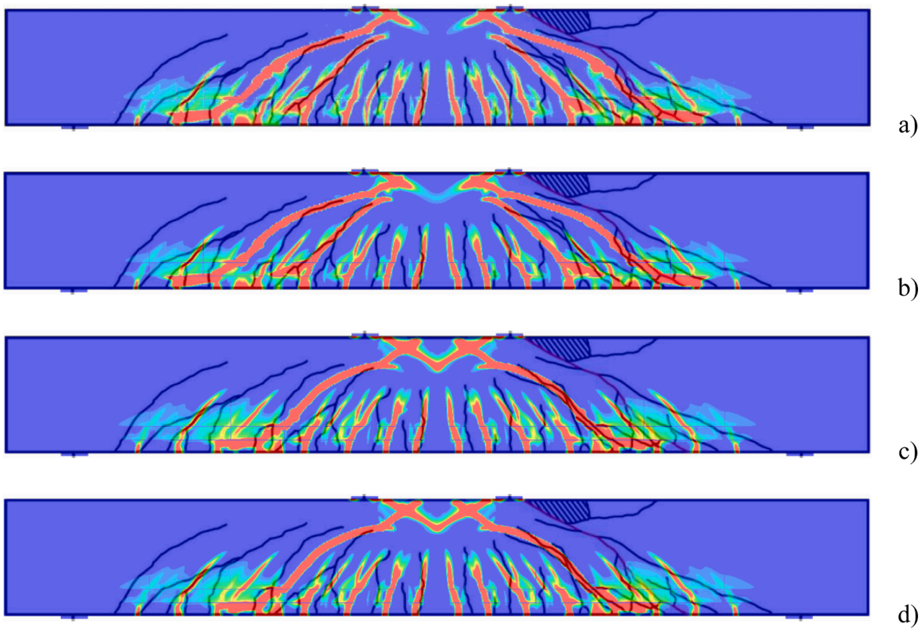

Fig. 23. Calculated force–deflection curves and distributions of non-local equivalent strain measure from 2D FE analyses as compared to experiments (beam S3D36A108, $\eta_a = 3.0$, $\rho_l = 4.3\%$) for different shear reinforcement ratio ρ_s: a) $\rho_s = 0.4\%$ (basic value), b) $0.75\rho_s$, c) $0.5\rho_s$, and d) $0.25\rho_s$.

6. Parametric numerical studies (based on beam series ‘3’)

6.1. Comparison between 2D and 3D simulations

Since the differences between the numerical and experimental results were the worst for the beam S3D36A54 ($D = 360$ mm, $a = 540$ mm, $L_{eff} = 1620$ mm, $\eta_a = 1.5$, $\rho_l = 4.3\%$, $\rho_s = 0.4\%$), some additional simulations were performed to improve the accordance between the results. Since the 2D simulations were not able to fully reflect the 3D effects expressed by e.g. concrete spalling due to the high horizontal compressive force, the 3D FE calculations were performed. The geometry of the 3D beam FE model is presented in Fig. 18. Similarly, as in 2D, the half part of the beam was taking into account to reduce the computational time. Approximately 3 million tetrahedral elements with linear shape functions were used with the maximum size about of $s_e = 4$ mm (Fig. 18). Assuming $l_c = 3$ mm ($s_e \leq 2l_c$), the material parameters used in 3D calculations were slightly modified to obtain similar values of fracture energies in both calculation types. The computation time increased by factor 10.

The calculated force–deflection curves and distributions on the non-local equivalent strain measure in 2D and 3D calculations are shown in Fig. 19. An evident improvement was observed in 3D simulations. The difference in the calculated ultimate vertical force dropped from 14% (2D conditions) down to 6% (3D conditions) (Fig. 19a). An improvement of the curve inclination in a hardening regime was also observed in 3D simulations. Instead of a diffused shear zone, a pronounced inclined localized zone was obtained at the shear-span (Fig. 19b). The location, shape and inclination of the critical diagonal shear localization zone were also closer to the experiment as compared with the 2D numerical approach. In summary, the 3D FE results provide more realistic results (in particular for higher RC beams), however, due to immense computation efforts, the 3D simulations are hardly applicable now for large RC beams. The 2D simulations are sufficiently realistic and hence they were used in the next section to perform a detailed parametric study.

6.2. Effect of reinforcement ratios for different shear span parameter

For investigating the influence of longitudinal and shear reinforcement ratios on the beams’ strength, an additional series of numerical calculations were performed (Figs. 20-26). The simulations in the

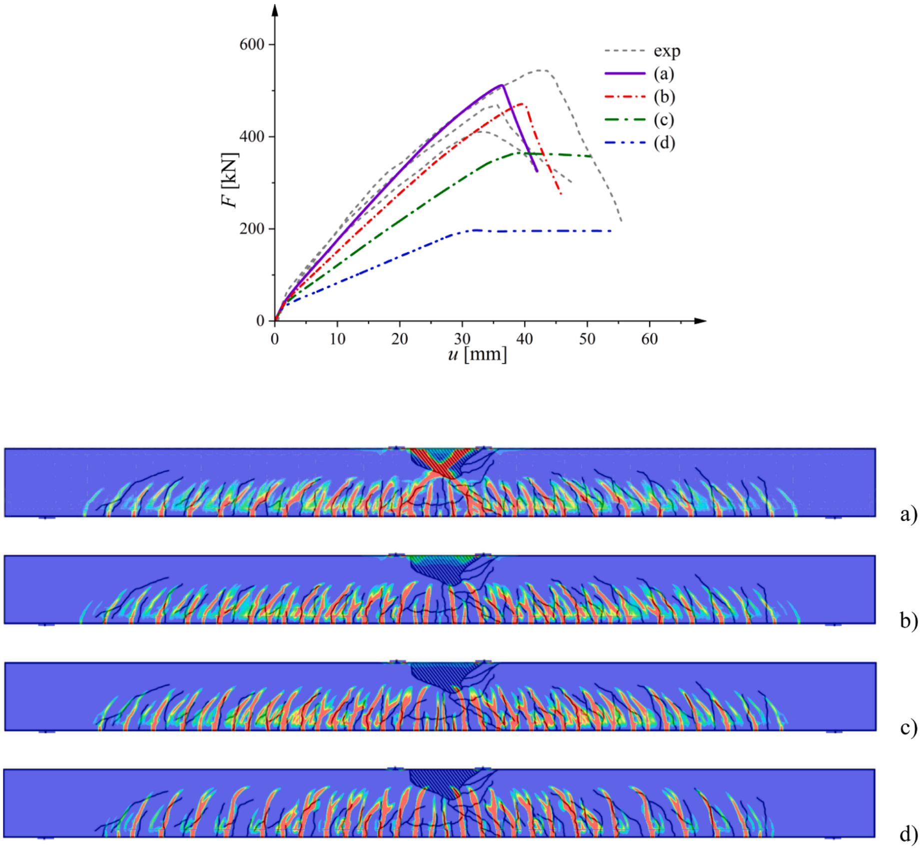

Fig. 24. Calculated force–deflection curves and distributions of non-local equivalent strain measure from 2D FE analyses as compared to experiments (beam S3D36A216, $\eta_a = 6.0$, $\rho_s = 0.4\%$) for different longitudinal reinforcement ratio ρ_l: a) $\rho_l = 4.3\%$ (basic value), b) $0.75\rho_l$, c) $0.5\rho_l$, and d) $0.25\rho_l$.

number of 24 were carried out for all beams of series ‘3’ with $\eta_a = 1.5$, 3.0 and 6.0 (D = 360 mm, t = 0.25 m). In FE calculations, a different longitudinal ratio ρ_l or transverse reinforcement ratio ρ_s was systematically reduced below $\rho_l = 4.3\%$, i.e. $0.75\rho_l$, $0.50\rho_l$ and $0.25\rho_l$ (with the experimental value $\rho_s = 0.4\%$) and below $\rho_s = 0.4\%$, i.e. $0.75\rho_s$, $0.50\rho_s$ and $0.25\rho_s$ (with the experimental value $\rho_l = 4.3\%$).

The reduction in the longitudinal reinforcement ratio contributed to a decrease of the ultimate vertical force and overall stiffness for all beams of series ‘3’ (Fig. 20, 22, 24 and 26A). The ultimate vertical forces decreased up to 50%-60% between $\rho_l = 4.3\%$ and $\rho_l = 0.25 \times 4.3\% = 1.075\%$ (Fig. 26A); the effect of the longitudinal reinforcement ratio ρ_l was more pronounced for the lower η_a. The failure type changed from shear-compression to reinforcement yielding for $\rho_l = 0.25 \times 4.3\% = 1.075\%$ with $\eta_a = 1.5$ (Fig. 20), from shear-compression to diagonal tension for $\rho_l = 0.75 \times 4.3\% = 3.22\%$ and to reinforcement yielding for $\rho_l \leq 0.50 \times 4.3\% = 2.15\%$ with $\eta_a = 3.0$ (Fig. 22) and from concrete crushing to reinforcement yielding for $\rho_l \leq 0.50 \times 4.3\% = 2.15\%$ with $\eta_a = 6.0$ (Fig. 24). Consequently, for the beams with $\eta_a = 1.5$ and 3.0, the decay of major critical shear localized zones took place connected with the development of bending localized zones of a pronounced height in the beam mid-part (Fig. 20d and 22d). For the beams with $\eta_a = 6.0$, the decay of a concrete crushing zone in the central upper beam region happened, followed by the development of more pronounced but less numerous bending localized zones (Fig. 24d). The rate of softening was similar in all failure mechanisms excluding reinforcement yielding; it was the highest for $\eta_a = 3.0$. The numerical results in Fig. 26A indicate that the reinforcement ratio might be decreased in experiments (Section 2) by 25% ($\eta_a = 3$ and $\eta_a = 6$) and 50% ($\eta_a = 1$) to avoid reinforcement yielding.

The effect of the shear reinforcement ratio ρ_s on shear strength was solely visible for the beams with $\eta_a = 3.0$ (Fig. 26B), wherein the ultimate vertical force decreased by 25% for $\rho_s = 0.1\%$ as compared to $\rho_s = 0.4\%$. The effect of the shear reinforcement ratio ρ_s on a failure mode and rate of softening was insignificant with $\rho_l = 4.3\%$. A reduction of the shear reinforcement ratio ρ_s influenced the position of a major critical inclined localized zone. For the smaller shear reinforcement ratio ρ_s, the larger distance from support was obtained (Fig. 23). The failure type changed from shear-compression ($\eta_a = 1.5$ and $\eta_a = 3.0$) to concrete crushing ($\eta_a = 6.0$) for $\rho_l \leq 4.3\%$ (Fig. 26B).

In summary, the structural strength should be related to a specific failure mode dependent on geometric parameters. The specification of the failure mode is fundamental in assessing the dependence of the limit load on design or redesign variables. The numerical FE calculations will be continued to find a full quantitative relationship between the shear strength related to a specific failure mode and parameters such as *D, L, t, a, b*, ρ_l, ρ_s, f_c and f_t (about 100 numerical simulations are foreseen).

7. Conclusions

The following basic conclusions can be derived from the experiments and FE analyses on the behaviour of RC beams with shear reinforcement which were scaled along with the height or length:

- The shear strength of experimental beams decreased with increasing parameter $\eta_a = a/D$. It also decreased with increasing parameter η_b from 0.75 to 2.5 in beams with varying effective depth and constant effective length.

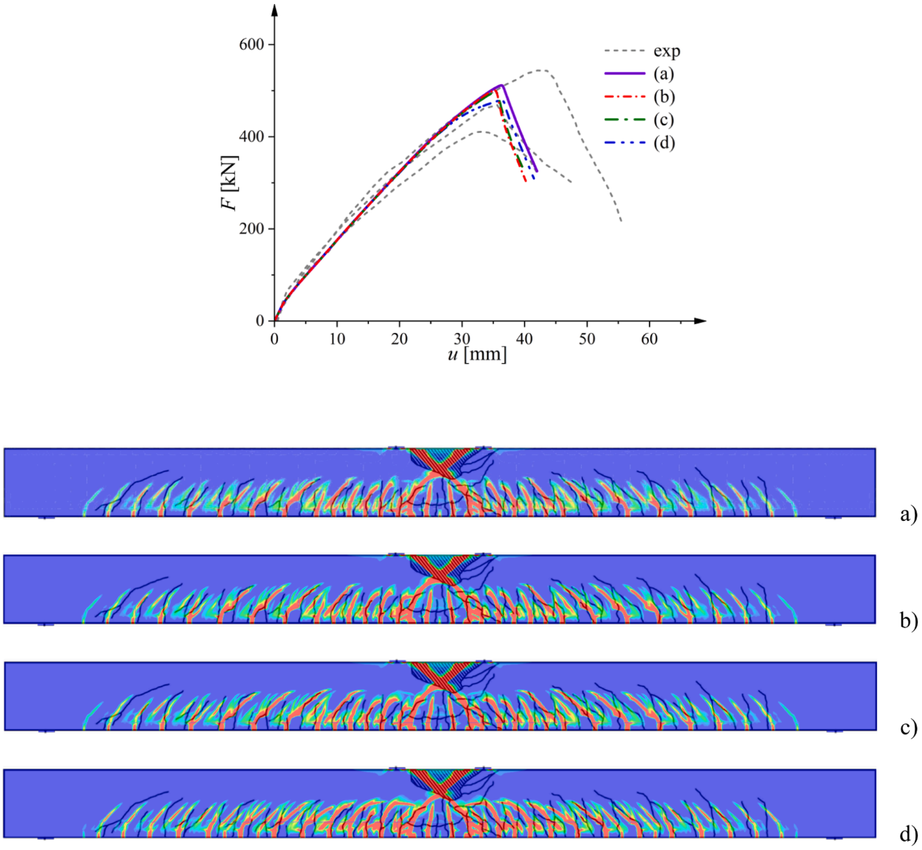

Fig. 25. Calculated force–deflection curves and distributions of non-local equivalent strain measure from 2D FE analyses as compared to experiments (beam S3D36A216, $\eta_a = 6.0$, $\rho_l = 4.3\%$) for different shear reinforcement ratio ρ_s: a) $\rho_s = 0.4\%$ (basic value), b) $0.75\rho_s$, c) $0.5\rho_s$, and d) $0.25\rho_s$.

- Two different basic failure modes were observed in RC beams with longitudinal and shear reinforcement during laboratory tests [22]. First, the concrete crushing in a compressive zone occurred in slender beams for $\eta_a = 5$–6 with the global quasi-brittle post-peak behaviour. As the reinforcement remained elastic, the compressive zone enlarged transversely and interacted with the cracked tensile zone in the final failure stage. Second, the brittle shear-compression failure was registered in beams for $\eta_a = 1.5$–3.0 where the critical diagonal crack developed with normal and tangential displacements of similar values. In the RC beams without stirrups [20], the reinforcement yielding occurred for $\eta_a = 6$, diagonal tension failure for $\eta_a = 2$–3 and shear-compression failure for $\eta_a = 1$–2. The presence of stirrups increased the beam strength by 130% for $\eta_a = 1.5$ (stirrups did not affect the failure mode) and 280% for $\eta_a = 3.0$ (stirrups changed the failure mode). A decrease of η_a due to the varying shear span a with the constant beam depth D had a slightly stronger effect on the beam shear strength than a decrease of η_a due to the varying D with $a = \text{const}$.
- The experimental results concerning strength, brittleness and fracture were realistically reproduced in FE calculations using a coupled elastic–plastic-damage model for concrete enhanced by a characteristic length of micro-structure within a non-local theory. The material constants were calibrated with accompanying standard laboratory tests. The differences between numerical and experimental outcomes grew with diminishing parameter η_a. The 3D simulations improved the numerical results concerning a load–deflection diagram and failure mode for high beams.
- The best prediction of the experimental shear strength of deep beams with $a/D = 1.5$ was obtained with the simple strut-and-tie model following ACI [60] (5%-error). The beam shear strengths of a transitional geometry $a/D = 2.5$–3.0 were also satisfactorily described with the same model (error of 1–15%) despite a different inclination of the critical diagonal shear crack. The strut-and-tie model proposed by Chen et al. [61] underestimated the shear strength of most beams (except the beam S3D36A54) by ca. 20%. The modified strut-and-tie model by Zhang and Tan [16] overestimated on the other hand the shear strength of all RC beams with $\eta_a = 1.5$–3 by 10–55%.
- The numerical beam strength and stiffness strongly increased with the growing longitudinal reinforcement ratio, in particular for the lower shear span parameters. The failure type changed from shear-compression to reinforcement yielding for $\eta_a = 1.5$, from shear-compression/diagonal tension to reinforcement yielding for $\eta_a = 3.0$ and from concrete crushing to reinforcement yielding for $\eta_a = 6.0$.
- The numerical beam strength increased with the growing transverse reinforcement ratio solely for the shear span parameter equal to 3 during shear-compression failure. The failure type changed from shear-compression ($\eta_a = 1.5$ and 3.0) to concrete crushing for $\eta_a = 6.0$.

Declaration of Competing Interest

The authors declare that they have no known competing financial interests or personal relationships that could have appeared to influence

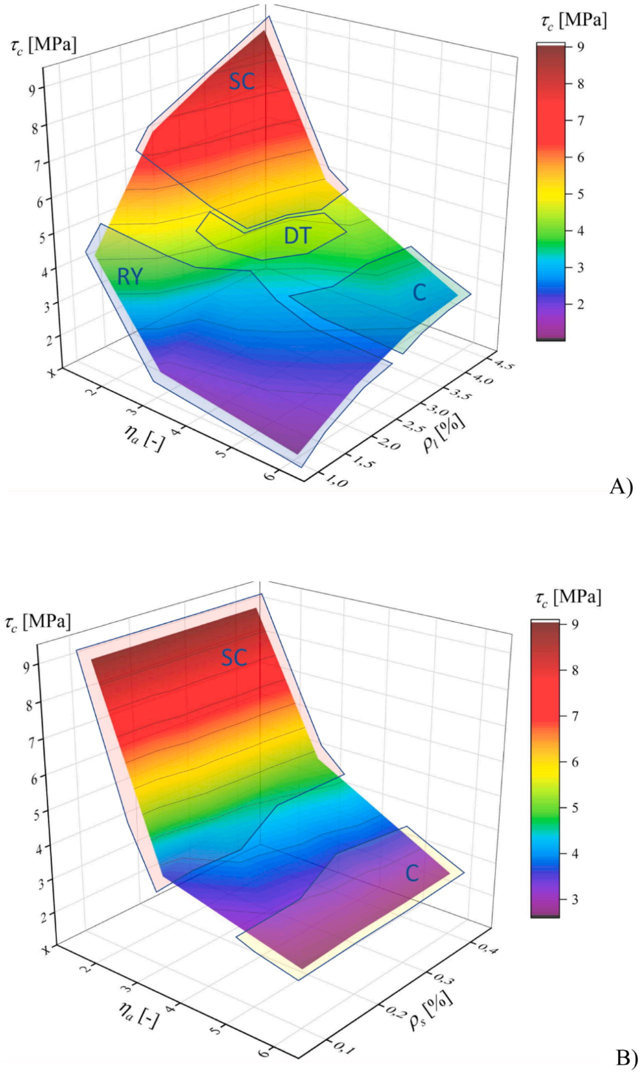

Fig. 26. 3D diagrams showing the effect of shear span ratio, main (A) and secondary reinforcement (B) ratio on strength and failure mode of RC beams (C - concrete compression, SC - shear-compression, DT - diagonal tension and RY - reinforcement yielding).

the work reported in this paper.

Acknowledgments

The research works have been carried out within the project: "*Experimental and numerical analysis of coupled deterministic-statistical size effect in brittle materials*" financed by the National Science Centre NCN (Narodowe Centrum Nauki) (UMO-2013/09/B/ST8/03598). The numerical calculations were performed on supercomputers of the Academic Computer Centre in Gdańsk TASK. The assistance of dr. habil. E. Korol and dr. J. Suchorzewski in the experiments' performance and evaluation is acknowledged. We thank prof. Z. Mróz for critical comments.

Appendix A

In Appendix, the analytical formulae used in Section 5 were summarized [22].

EN 1992-1-1 (2008) [58]

The shear strength of RC beams with stirrups is calculated based on the variable inclination truss analogy. The shear resistance for non-prestressed members should be taken to be less than:

$$V_{Rd,s} = \frac{A_{sw}}{s} z f_{ywd} cot\theta \text{ (shear reinforcement yielding)} \quad \text{(A1)}$$

or

$$V_{Rd,max} = \frac{tz\nu_1 f_{cd}}{(cot\theta + tan\theta)} \text{ (concrete crushing)}, \tag{A2}$$

where the recommended strut inclination is $1 \le \cot\theta \le 2.5$, A_{sw} - the cross-section area of one stirrup, f_{ywd} - the yield strength of stirrups, s denotes the stirrup spacing, f_{cd} - the design concrete compressive strength, ν_1 - the empirical coefficient of the cracked concrete shear strength ($\nu_1 = 0.6$ for the characteristic concrete strength $f_{ck} < 60$ MPa) and z - the internal lever arm ($z \cong 0.9D$ for bending).

ACI 318-14 (2014) [60]

The shear strength of deep RC beams according is calculated by applying a simple strut-and-tie model with the strut inclination angle θ_s defined as $\tan\theta_s = D/a$. The formula is applicable for the ratio $\eta_a \le 2.0$. The shear strength of beams is governed by the minimum from the strut compressive strength F_{ns}, the tie tensile strength F_{nt} and the compressive strength of the nodal zone F_{nn}. Generally in deep beams, the strut is the weakest component and the resultant ultimate vertical force V_n and corresponding shear strength $\tau_c = V_n/A_c$ are calculated as

$$V_n = F_{ns} sin\theta_s \tag{A3}$$

and

$$\tau_c = (f_{ce}A_{cs}) sin\theta_s / A_c, \tag{A4}$$

where f_{ce} - the effective strut compressive strength and $A_{cs} = w_s t$ - the cross-sectional area at the strut end, $A_c = tD$ – the effective cross-sectional area of a beam. The strut width w_s depends on the supporting plate geometry and longitudinal reinforcement arrangement:

$$w_s = l_c cos\theta_s + l_b sin\theta_s. \tag{A5}$$

where l_b - the supporting plate length and l_c - the height of the CCT node depending on the concrete cover and number of reinforcement layers. The presence of stirrups is taken into account by modifying the effective compressive strength of concrete in the strut $f_{ce} = 0.85\beta_s f'_c$ with $\beta_s = 0.75$ (in the beams without transverse reinforcement $\beta_s = 0.6$). Equation A(4) can be transformed (by substituting $l_b = l_c \text{tg}\theta_s$) as

$$\tau_c = 2f_{ce}\eta_c/\eta_a = 1.7\beta_s f_c'\eta_c/\eta_{a.} \tag{A6}$$

The shear strength in Eq.A6 is affected by two size parameters η_a and η_c (the shear strength increases with decreasing η_a and increasing η_c) and one material parameter f_{ce} that takes into account the concrete strength and presence of stirrups. The nominal strength of the nodal zone was calculated as $F_{nn} = f_{ce}A_{nz}$ with $f_{ce} = 0.85 f_c'\beta_n$ ($\beta_n = 0.8$ for the CCT node and $\beta_n = 1.0$ for the CCC node) wherein A_{nz} - the node face area perpendicular to the strut direction.

Formulae by Zhang and Tan [16]

Zhang and Tan [16] improved a strut-and-tie model by taking into account the Mohr-Coulomb failure condition in a tension–compression stress state and a contribution of the bottom reinforcement to the strut compression. The formula again remains valid as long as $\eta_a \le 2.0$. The ultimate force V_n in RC beams may be determined from the formula:

$$V_n[\frac{4sin\theta_s cos\theta_s}{f_t A_c} + \frac{sin\theta_s}{f_c A_{str}}] = 1, \tag{A7}$$

where $A_c = d_c t$ is the effective cross-sectional area of a beam ($d_c = D\text{-}0.5l_d$), $A_{str} = w_s t$ is the cross-sectional area of the strut. The width of strut w_s is calculated in the same way as in ACI but with a slightly modified strut inclination angle θ_s defined as $\tan\theta_s = d_c/a$. The maximum tensile strength f_t of the bottom nodal zone is calculated as the sum of three components:

$$f_t = \frac{4A_s f_y sin^2\theta_s}{A_c} + \frac{f_{ywd}A_{sw} sin(\theta_s + \theta_w)}{A_c/sin\theta_s} + 0.31\sqrt{f_c}(\frac{\varepsilon_{cr}}{\varepsilon_1})^{0.4} \tag{A8}$$

The first component in Eq.A8 results from the main longitudinal reinforcement action, the second part takes into account the effect of shear reinforcement (θ_w - the inclined angle of shear reinforcement with respect to the horizontal line) and the third component considers the cracked concrete tensile strength (ε_{cr} - the concrete strain during cracking taken as 0.00008, ε_1 - the principal tensile strain of the concrete strut ($\varepsilon_1 = \varepsilon_s + (\varepsilon_s + \varepsilon_2)\text{ctg}2\theta_s$, ε_s and ε_2 - the tensile strain of longitudinal reinforcement and peak compressive strain of the concrete strut at crushing). The tensile strain ε_s depends on the compressive zone height and is calculated in an iterative procedure. Thus, the ultimate force resulting from Eq.A8 (or the corresponding shear strength) cannot be expressed in a straightforward manner by the size parameters η_a, η_b and η_c as it in the case of Eq.A7. The ultimate force in Eq.A8 depends on six geometric parameters (D, t, c', A_s, A_{sw}, θ_s, and l_d) and five material parameters (f_y, f_{ywd}, f_c, ε_{cr}, and ε_1).

Formulae by Chen et al. [61]

The strut-and-tie model applies to deep beams with $\eta_a \le 2.5$. It assumes the strut of the width w_s consisting of a cracked and un-cracked part that transfer the following ultimate forces:

$$F_{si} = \sigma_{ci}w_{si}t = \kappa_c\beta_{si}f_c^{'}w_{si}t \tag{A9}$$

$$F_{sc} = \sigma_{cc}w_{sc}t = \beta_{sc}f_c^{'}w_{sc}t \tag{A10}$$

The non-cracked part of the width w_{si} and cracked part of the width w_{sc} have the effective compressive strengths $\sigma_{si} = \kappa_c\beta_{si}f'_c$ and $\sigma_{sc} = \beta_{sc}f'_c$, respectively ($f'_c$ is the cylindrical concrete compressive strength, $\kappa_c = 1\text{-}f'_c/250$ and $\beta_{si} = 0.85$). The strut efficiency coefficient β_{sc} takes into account the aggregate interlocking, dowel action of longitudinal bars and shear reinforcement strength. The value of β_{sc} is found through an iterative procedure with the initial value of $\beta_{sc} = 0.85$. The ultimate force of deep beams is obtained as the sum of F_{si} and F_{sc}:

$$V_n = (F_{si} + F_{sc}) sin\theta_s \tag{A11}$$

where the strut angle tanθ_s=$(D\text{-}c/2)/a$ is the function of the effective beam depth D, shear span a and nodal CCC zone height c. The compression zone depth c can be found using the linear flexural theory (the concrete compressive strength in the compression zone at the mid-span does not reach its ultimate strength). The solution of equation $c^2 + 2n\rho Dc\text{-}2n\rho D^2 = 0$ (with $n = E_s/E_c$) derived from the equilibrium condition of a plane section provides the compression zone height c. The ultimate force (or corresponding shear strength) in Eq.A11 cannot be presented as an explicit function of the size parameters η_a , η_b and η_c due to an iterative procedure used to determine the strut efficiency coefficient β_{sc}. The ultimate shear strength of deep beams in Eq.A11 depends on ten geometric parameters (D, t, b, c, l_{bt}, θ_s, α, ρ, $\rho\nu$ and ϕ_s) and five material parameters (κ_c, β_{si}, f'_c, E_s and E_c).

Flexural strength

The ultimate flexural strength of beams with $\eta_a \geq 2.5$ failing due to concrete crushing in the compression zone was estimated from the equilibrium conditions in the beam section. Assuming a simplified rectangular stress distribution in the compression zone, the lever arm is $z = D(1\text{–}0.5\xi_{eff,lim})$ with $\xi_{eff,lim} = 0.8 \times 0.0035/(0.0035 + E_c/E_s)$. The ultimate vertical force reads as follows:

$$V_{n,flex} = \frac{\alpha f_c t D^2 \mu_{eff,lim}}{a} \tag{A12}$$

with $\mu_{eff,lim} = \xi_{eff,lim}(1\text{–}0.5\xi_{eff,lim})$ and $\alpha = 0.85$.

References

[1] Bažant ZP, Planas J. Fracture and size effect in concrete and other quasi-brittle materials. CRC Press LCC 1989.
[2] Carpinteri A. Decrease of apparent tensile and bending strength with specimen size: two different explanations based on fracture mechanics. Int J Solids Struct 1989;25(4):407–29.
[3] Duan K, Hu Z. Specimen boundary induced size effect on quasi-brittle fracture. Strength Fract Complexity 2004;2(2):47–68.
[4] Bažant ZP, Pang S-D, Vořechovský M, Novák D. Energetic-statistical size effect simulated by SFEM with stratified sampling and crack band model. Int J Numer Methods Eng 2007;71(11):1297–320.
[5] Walraven JC. The influence of depth on the shear strength of lightweight concrete beams without shear reinforcement, Stevin Laboratory Report No.5-78-4, Delft University of Technology, vol. 36 (1978).
[6] Bažant ZP, Kazemi MT. Size effect on diagonal shear failure of beams without stirrups. ACI Struct J 1991;88(3):268–76.
[7] Kim JK, Park YD. Shear strength of reinforced high-strength concrete beams without web reinforcement. Mag Concr Res 1994;46(166):7–16.
[8] Tan KH, Lu HY. Shear behaviour of large reinforced concrete deep beams and code comparisons. ACI Struct J 1999;96(5):836–45.
[9] Angelakos D, Bentz EC, Collins MP. Effect of concrete strength and minimum stirrups on shear strength of large members. ACI Struct J 2001;98(3):290–300.
[10] Yang K-H, Chung H-S, Lee E-T, Eun H-C. Shear characteristics of high-strength concrete deep beams without shear reinforcements. Eng Struct 2003;25(10):1343–52.
[11] Reineck KH, Kuchma D, Kim KA, Marx S. Shear database for reinforced concrete members without shear reinforcement. ACI Struct J 2003;100(2).
[12] Lubell A, Sherwood T, Bentz E, Collins M. Safe shear design of large, wide beams. Concr Int 2004;26(1):66–78.
[13] Tan KH, Cheng GH, Cheong HK. Size effect in shear strength of large beams-behaviour and finite element modelling. Mag Concrete Res 2005;57(8):497–509.
[14] Syroka-Korol E, Tejchman J. Experimental investigations of size effect in reinforced concrete beams failing by shear. Eng Struct 2014;58:63–78.
[15] Walraven JC, Lehwalter N. Size effects in short beams loaded in shear. ACI Struct J 1994;91(5):585–93.
[16] Zhang N, Tan KH. Size effect in RC deep beams: Experimental investigation and STM verification. Eng Struct 2007;29:3241–54.
[17] Belgin ÇM, Şener S. Size effect on failure of overreinforced concrete beams. Eng Fract Mech 2008;75(8):2308–19.
[18] Carpintieri C, Carmona JR, Ventura G. Failure mode transitions in reinforced concrete beams. Part 2: Experimental tests. ACI Struct J 2011;108:286–93.
[19] Słowik M, Smarzewski P. Study of the scale effect on diagonal crack propagation in concrete beams. Comput Mater Sci 2012;64:216–20.
[20] Suchorzewski J, Korol E, Tejchman J, Mróz Z. Experimental study of shear strength and failure mechanisms in RC beams scaled along height or length. Eng Struct 2018;157:203–23.
[21] Marzec I, Tejchman J, Mróz Z. Numerical analysis of size effect in RC beams scaled along height or length using elasto-plastic-damage model enhanced by non-local softening. Finite Elem Anal Des 2019;157:1–20.
[22] Korol E, Suchorzewski J, Tejchman J, Mróz Z. Experimental investigations of shear strength and failure mechanisms in RC beams with stirrups scaled along with height or length. Internal Report, Gdansk University of Technology 2020.
[23] Kani GNJ. The basic facts concerning shear failure. Proc ACI J 1966;63(7):675–92.
[24] Krajcinovic D, Fonseka G. The continuous damage theory of brittle materials. J Appl Mech ASME 1981;48(4):809–24.
[25] Mazars Jacky. A description of micro- and macroscale damage of concrete structures. Eng Fract Mech 1986;25(5-6):729–37.
[26] Simo JC, Ju J. Strain- and stress-based continuum damage models. Int J Solids Struct 1987;23(7):821–40.
[27] Lubliner J, Oliver J, Oller S, Oñate E. A plastic-damage model for concrete. Int J Solids Struct 1989;25(3):299–326.
[28] Meschke G, Lackner R, Mang HA. An anisotropic elastoplastic-damage model for plain concrete. Int J Numer Methods Eng 1998;42(4):703–27.
[29] Faria R, Oliver J, Cervera M. A strain-based plastic viscous-damage model for massive concrete structures. Int J Solids Struct 1998;35(14):1533–58.
[30] E. Hansen, K. Willam, A two-surface anisotropic damage-plasticity model for plane concrete, Proceedings Int. Conf. Fracture Mechanics of Concrete Materials, R. de Borst [Ed.], Paris, Balkema, 549–56, 2001.
[31] Chen JF, Morozov EV, Shankar K. A combined elastoplastic damage model for progressive failure analysis of composite materials and structures. Compos Struct 2012;94(12):3478–89.
[32] Grassl P, Xenos D, Nyström U, Rempling R, Gylltoft K. CDPM2: A damage-plasticity approach to modelling the failure of concrete. Int J Solids Struct 2013;50:3805–16.
[33] Mihai J, Jefferson A, Lyons L. Plastic-damage constitutive model for the finite element analysis of fibre reinforced concrete. Eng Fract Mech 2016;159:35–62.
[34] Xotta G, Beizaee S, Willam KJ. Bifurcation investigations of coupled damage-plasticity models for concrete materials. Comput Methods Appl Mech Eng 2016;298:428–52.
[35] Marzec I, Tejchman J. Computational modelling of concrete behaviour under static and dynamic conditions. Bull Polish Acad Sci - Tech Sci 2013;61(1):85–96.
[36] Pamin J, de Borst R. Stiffness degradation in gradient-dependent coupled damage-plasticity. Arch Mech 1999;51(3–4):419–46.
[37] Marzec Ireneusz, Skarzynski Lukasz, Bobinski Jerzy, Tejchman Jacek. Modelling reinforced concrete beams under mixed shear-tension failure with different continuous FE approaches. Comput Concr 2013;12(5):585–612.
[38] Skarżyński L, Marzec I, Tejchman J. Experiments and numerical analyses for composite RC-EPS slabs. Comput Concr 2017;20(6):689–704.
[39] Skarżyński L, Marzec I, Drąg K, Tejchman J. Numerical analyses of novel prefabricated structural wall panels in residential buildings based on laboratory tests in scale 1:1. Eur J Environ Civil Eng 2020;20(9):1450–82.
[40] Marzec I, Bobiński J, Tejchman J, Schönnagel J. Finite element analysis on failure of reinforced concrete corner in sewage tank under opening bending moment. Eng Struct 2021;228:111506. https://doi.org/10.1016/j.engstruct.2020.111506.
[41] Marzec I, Bobiński J. Performance of isotropic constitutive laws in simulating failure mechanisms in scaled RC beams. Arch Mech 2020;72(3):193–215.
[42] Peerlings RHJ, de Borst R, Brekelmans WAM, Geers MGD. Gradient enhanced damage modelling of concrete fracture. Mech Cohesive-Frict Mater 1998;3(4):323–42.
[43] Geers MGD. Experimental analysis and computational modeling of damage and fracture. PhD Thesis. Eindhoven University of Technology; 1997.
[44] Lee Jeeho, Fenves Gregory L. Plastic-damage model for cyclic loading of concrete structures. J Eng Mech 1998;124(8):892–900.
[45] Carol Ignacio, Willam Kaspar. Spurious energy dissipation/generation in stiffness recovery models for elastic degradation and damage. Int J Solids Struct 1996;33(20-22):2939–57.
[46] Pijauder-Cabot G, Bažant ZP. Non-local damage theory. ASCE J Eng Mech 1987;113:1512–33.
[47] Bažant Zdeněk P, Jirásek Milan. Non-local integral formulations of plasticity and damage: survey of progress. J Eng Mech 2002;128(11):1119–49.
[48] Bobinski J, Tejchman J. Numerical simulations of localization of deformation in quasi-brittle materials within non-local softening plasticity. Comput Concr 2004;1(4):433–55.

[49] Bobiński J, Tejchman J. Comparison of continuous and discontinuous constitutive models to simulate concrete behaviour under mixed mode failure conditions. Int J Numer Analyt Methods Geomech 2016;40:406–35.

[50] Borino G., Failla, F. Parrinello F. A symmetric formulation for non-local damage models, In Mang HA, Rammerstorfer FG, Eberhardsteiner J. (eds). Proc. of 5th World Congress on Computational Mechanics (WCCM V), Vienna, Austria, 2002. Vienna University of Technology. ISBN 3-9501554-0-6, http://wccm.tuwien.ac.at.

[51] Tejchman J, Bobiński J. Continuous and discontinuous modeling of fracture in concrete using FEM. Berlin-Heidelber: Springer; 2013.

[52] Mahnken R, Kuhl E. Parameter identification of gradient enhanced damage models. Eur J Mech A/Solids 1999;18:819–35.

[53] Skarżyński Ł, Syroka E, Tejchman J. Measurements and calculations of the width of fracture process zones on the surface of notched concrete beams. Strain 2011;47:319–32.

[54] CEB-FIP, CEB-FIP model code 1990, 1993.

[55] Korol E, Tejchman J, Mróz Z. Experimental and numerical assessment of size effect in geometrically similar slender concrete beams with basalt reinforcement. Eng Struct 2017;141:272–91.

[56] Abaqus Documentation (2016), Dassault Systemes.

[57] Syroka-Korol E, Tejchman J, Mróz Z. FE analysis of size effects in reinforced concrete beams without shear reinforcement based on stochastic elasto-plasticity with non-local softening. Finite Elem Anal Des 2014;88:25–41.

[58] EN 1992-1-1: Design of concrete structures: Part 1-1: General rules and rules for buildings.

[59] ACI 435R-95: Control of Deflection in Concrete Structures, American Concrete Institute, 2000.

[60] ACI 318-14: Building code requirements for structural concrete, American Concrete Institute, 2014.

[61] Chen H, Yi W, Hwang HJ. Cracking strut-and-tie model for shear strength evaluation of reinforced concrete deep beams. Eng Struct 2018;163:396–408.

[62] Skarżyński Ł, Marzec I. Shear fracture of longitudinally reinforced concrete beams under bending using Digital Image Correlation and FE simulations with concrete micro-structure based on X-ray micro-computed tomography images. Constr Build Mater 2021;274:122116. https://doi.org/10.1016/j.conbuildmat.2020.122116.